Spring 2016

Physical Chemistry of Atmospheric Aerosols: From Iron Leaching to the Design of Interface Experiments

Jaya Borgatta
Skidmore College, jborgatt@skidmore.edu

Physical chemistry of atmospheric aerosols: from iron leaching to the design of interface experiments

Jaya Borgatta

Spring 2016

Skidmore College

Chemistry Department

Acknowledgments

I would like to thank Professor Frey for reading this document and providing valuable comments and advisement. I would like to thank Professor Navea for being both advisor and mentor.

Table of Contents

Chapter 1: Atmospheric interfaces: introduction and motivation.

Atmospheric aerosols are particles with a wide variety of composition and morphology, that can serve as complex environmental interfaces for heterogeneous chemistry.[1-3] Due to their prevalence in the lower atmosphere, these aerosol particles can have uncertain effects on global climate and biogeochemical cycles.[2] In chapter two of this work, we have explored the fate of atmospheric particles by investigating the dissolution of iron from anthropogenic aerosols. The study determined the leach rate of iron (II) and iron (III) from fly ash (FA), an anthropogenic aerosol produced by the combustion of coal. Our findings indicate that the leach rate and relative quantities of iron species would depend upon the source region of FA. Atmospheric iron was further studied by looking at the interactions of iron with atmospheric organic chelating and reducing organic agents, humic-like substances (HULIS). Humic-like substances were seen to interact with iron and reduce Fe (III). In addition, chapter four introduces the design and optimization of state-of-the-art instrumentation for the study of photochemistry and free radical reactions on atmospheric aerosol components. Finally, the present work describes the development of surface experiments designed to better understand the weathering influence of solar radiation and hydroxyl radicals on atmospheric aerosols.

Complex environmental interfaces: tropospheric aerosols

Aerosols are small solid or liquid particles suspended predominantly in the troposphere, the lowest layer of the atmosphere extending from the surface of Earth to 16 km above the earth's surface.[2] In general, the formation and atmospheric fate of aerosols is influenced by natural phenomena and anthropogenic activities that occur on the Earth's surface.[4] In general, aerosol properties, such as morphology and minerology, depend upon the type, source region, and weathering processes of the particles.[5] It is important to understand the charachterisitics of aerosol

particles, as the effects that aerosols can have on climate, biogeochemical cycles, and the chemical balance of the atmosphere, varies widely with the aerosol particle properties.[2] The various properties of natural and anthropogenic aerosols leave a distinct impact on the natural environment.

Naturally occurring atmospheric aerosols can be produced from ocean spray, volcanic activity, forest fires, and desert dust.[3] The expansive deserts of Asia and Africa contribute with the largest fraction of natural aerosol mass annually, an estimated emission of 800–2000 Tg.[6] Despite the prevalence of naturally-produced particulate matter in the atmosphere, a large fraction of aerosols are produced by human activity.[7]

Anthropogenic aerosols are generated predominantly by fuel combustion processes.[8] When fuels are combusted, small particles are produced and released into the atmosphere.[7] In particular, the combustion of coal results in the production of fly ash particles that are typically small, spherical, and have a long atmospheric residence time. The properties of fly ash particles facilitate long distance atmospheric transport; for instance, fly ash particles have been identified in air samples collected over isolated regions of the ocean.[9] Thus, fly ash particles have been deposited on the surface of the ocean or land far from the power plant that produced them.[10] Figure 1.1 shows an aerosol plume emitted from Calcutta, India, with a high content of fly ash.

Figure 1.1. Fly ash plume over northern India, transported towards Bangladesh and the Bengal Bay. Image obtained from NASA MODIS satellite.

Fly ash transport happens on a global scale with a moderately long atmospheric lifetimes.[2] As is clear from the image in Figure 1.1, the plume of aerosols rich in fly ash, while originated in Calcutta, India, is observed mostly over Bangladesh. As fly ash is deposited, its effects can be seen in Figure 1.1 as an intense green coloration in the Bay of Bengal.

Atmospheric iron and deposition

The weathering and deposition of fly ash and other atmospheric aerosols has been associated with changes in biogeochemical cycles.[11] Specifically, fly ash has been suggested to have a stimulatory effect on phytoplankton growth by leaching iron into aerosol droplets with the subsequent deposition into the ocean. In these regions, biologically available iron (II) acts as a limiting nutrient for phytoplankton. Therefore, fly ash having a large fraction of iron, could induce eutrophication in remote regions of the ocean.[12] Figure 1.2 shows a relatively high correlation between phytoplankton blooms and tropospheric aerosols.[13] Phytoplankton growth influences climate as a whole, because the growth of phytoplankton sequesters CO_2 from the atmosphere. Thus, the production and wet deposition of fly ash may have net global cooling effect.

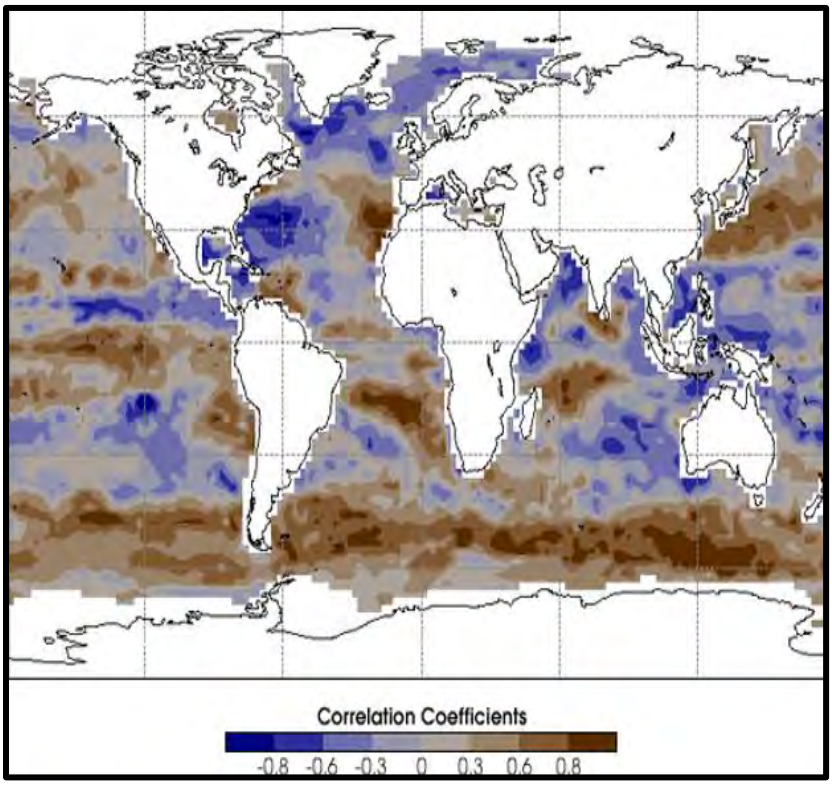

Figure 1.2. Phytoplankton blooms stimulated by the deposition of aerosols.[13]

Previous studies have been performed that have looked at the leach rate of iron from mineral dust, within the context of the iron hypothesis. Mineral dust shows a higher fraction of reduced trace metal species when compared to combustion particles, which are generated through a highly oxidative process. In fact, proton-promoted iron dissolution from mineral dust have shown a relatively important fraction of Fe(II), ranging between 5 to 38% of the total iron leached from mineral dust, depending on the source region.[14] This relatively large fraction of Fe(II) has the potential to impact the bioavailable iron mobility in the environment. Thus, a complimentary study on the effect of combustion particles such as fly ash, from distinctive sources and power plants, is important to establish its effect on the environmental availability of iron.[14]

The stimulatory effects of fly ash on phytoplankton is dependent upon particle size and minerology.[8] Globally, the fly ash that is produced has a high degree of variability, depending upon the coal source region, the combustion process employed, and the processing of the fly ash. For instance, the duration of the combustion process may result in different varieties of metal oxides. In addition, the coal minerology will differ depending on the source region which will also influence the elemental composition of the fly ash that is produced.[7] Thus, the chemical composition of fly ash is dependent upon source region and source power plant. In this study, we aim to observe the iron leach rate from authentic fly ash samples sourced from three distinctive regions: India, Europe, and the United States.

Given the oxidizing process that produces it, iron leached from fly ash may be predominantly Fe (III), with trace amounts of Fe(II). However, only Fe (II) is biologically available and can stimulate phytoplankton growth. Therefore, it is important to investigate the presence of naturally occurring reducing agents that may facilitate the conversion of Fe (III) to Fe (II). Humic like substances (HULIS) are powerful redox and chelating species found in the atmosphere.[15, 16]

Humic like substances are complex organic acids produced by vegetative decay, that may be introduced to the atmosphere through agricultural practices, secondary formation, and the combustion of biomass.[15, 16] The redox potential of these aerosols make them relevant to the study of fly ash.[17] In this study, we have examined the abaility of HULIS to chelate F(II) and Fe(III) employing a cation exchange with Al(III) to determine the strength of the interaction, and its effect on the reduction of Fe(III) to bioavailable Fe(II).

Heterogeneous chemistry and photochemistry on aerosol particles

Aside from acting as the source of biologically relevant materials, aerosol particles can also facilitate reactions during their atmospheric weathering process.[18-20] Atmospheric weathering depends upon the composition of the observed particles and the reactants that they come in to contact with.[21] Typically, atmospheric particles consist of metal oxides, alumino-silicates, clays, and a variety of organic species.[22] In particular, the optical properties of some metal oxides can induce surface reactions due to their semiconducting properties.[1, 18] A semiconductor has a small enough band gap to promote electrons from the valence band to the conduction band, which means that they can provide an electron-hole pair to facilitate other reactions.[1, 18, 23] The weathering reactions for aerosol particles are typically due to interactions with light, acidic media, sulfur dioxide, nitrogen oxides, and hydroxyl radicals.[1, 18, 22]

In particular, hydroxyl radicals are a powerful and prevalent weathering agents.[24] Hydroxyl radicals are believed to facilitate the oxidation of organic aerosol components.[25] Previous studies have investigated the reaction between hydroxyl radicals and organic species adsorbed onto metal oxide surfaces.[25] However, the aforementioned studies relied upon the use of UV-light to generate the desired radical species, therefore, the authors were unable to discern whether the products of their reactions were due to interactions with light or the donation of electrons excited from the

semiconducting surface. To independently study the influence of hydroxyl radicals in the absence of light, a state of the art system was designed using a plasma as the source of radical species. Plasma is ionized gas that consists of radical species and electrons. For our reactions a low pressure system was used to generate a non-thermal plasma. The low pressure prevents the collisions and recombination the radical species and the respective electrons.

To validate the reaction system, preliminary experiments were performed to test the pressure dependence of the system and to see whether a benzaldehyde sample adsorbed to aluminum oxide would undergo an oxidation process. In addition, the influence of light on the reaction on nitric acid, a trace atmospheric gas, adsorbed to semiconducting surfaces was also studied.[1] To determine whether the desorbed reaction products underwent any further reactions due to light before reaching the detector, the irradiance profile of the solar simulator was determined and related to the diffusion rates of gases.

In the following pages we have observed the iron leach rate of authentic fly ash samples to determine the influence of source region within the context of the iron hypothesis. We determined whether iron (III) leached may be reduced in the presence of HU-LIS to form biologically available iron (II). In addition, we developed systems to study the reactions of organic compounds adsorbed to semiconducting surfaces to discern the influence of hydroxyl radicals and light.

References

1. Lesko, D. M. B., Coddens, E. M, Swomley, H. D., Welch, R. M, Borgatta, J. and Navea, J. G. *Phys. Chem. Chem. Phys.* **2015**, 17, 20775 - 20785
2. Seinfeld, J. H. & Pandis , S. N., *Atmospheric Chemistry and Physics: From Air Pollution to Climate Change* **2006,** (Wiley, Hoboken, N. J.).
3. Finlayson-Pitts, B. J. *Phys. Chem. Chem. Phys.* **2009,** 11, 7760-7779.
4. Usher, C. R.; Michel, A. E. and Grassian, V. H. *Chem. Rev.* **2003,** 103 (12), 4883–494.

5. Navea, J. G.; Chen, H.; Huang, M.; Carmichel, G. R. & Grassian, V. H. *Environ. Chem.* **2010, 7**, 162-170.
6. Prather, K. A.; Hatch, C. D. & Grassian, V. H., *Annu. Rev. Analytical Chem.* **2008,** 1, 485-514.
7. Chen, H.; Laskin, A.; Baltrusaitis, J.; Gorski, C. A.; Scherer, M. M.; Grassian, V. H. *Environ. Sci. Tech.* **2012,** 46, 2112-2120.
8. Iwashita, A.; Nakajima T.; Takanashi, H.; Ohki, A., Fujita, Y.; Yamashita, T. *Talanta* **2007,** 71, 251-257.
9. Srinivas, B.; Sarin, M. M.; Kumar, A. *Biogeochemistry* **2012**, 110 (1), 257-268.
10. Ramanathan, V.; Crutzen, P. J.; Kiehl, J. T.; Rosenfeld, D. *Science* **2001,** *294* (5549), 2119-2124.
11. Martin, J. H. *Paleoceanography* **1990,** 5 (1), 1-13.
12. Chen, H. and Grassian, V. H. *Environ. Sci. Technol.* **2013,** 47, 10312−10321.
13. Erickson, D. *Am. Geophys. Un*. San Francisco, CA, 2000. A52G-07.
14. Cwiertny, D.; Baltrusaitis, J.; Hunter, G. J.; Laskin, A.; Scherer, M.; Grassian, V. H. *J. Geophys. Res.* **2008,** 113, D05202.
15. Graber, E. R. & Rudich, Y. *Atmos. Chem. Phys.* **2006,** 6, 729-753.
16. Borgatta, J. & Navea, J. G. *WIT Transact. Ecol.Environ.* **2015,** 198, 155-166.
17. Aeschbacher, M.; Sander, M.; and Schwarzenbach, R. P. *Environ. Sci. Tech.*, **2010,** 44, 87–93.
18. Chen, H. H.; Navea, J. G.; Young, M. A.; Grassian, V. H. *J. Phys. Chem. A.* **2011,** 115, 490-499.
19. Rubasinghege, G.; Elzey, S.; Baltrusaitis, J.; Jayaweera, P. M.; Grassian, V. H. *J. Phys. Chem. A. Letters* **2010**, *1*, 1729-1737.
20. Finlayson-Pitts, B. J.; Raff, J. D.; Njegic, B.; Kamboures, M. A.; Chang, W.; Dabdub, D.; Gerber, R. B. *Abstr. Pap. Am. Chem. S.* **2009**, *237*, 177-177.
21. Claquin, T.; Schulz, M.; Balkanski, Y. J. " *J. Geophys. Res-Atmo*. **1999**, *104*, 22243-22256.
22. Navea, J. G.; Huang, M.; Carmichael, G. R.; Grassian, V. H. *Environ. Chem*. **2010**, 7, 162-170.
23. Ancutiene, I.; Navea, J. G.; and Baltrusaitis, J. *App. Surf. Sci.* **2015***,* 347, 520–527
24. Rudich Y.; Donahue N. M.; Mentel T.F. *Annu. Rev. Phys. Chem*. **2007**, 58:321-52.
25. Palm, B. B.; Campuzano-Jost, P.; Ortega, A. M.; Day, D. A.; Kaser, L.; Jud, W.; Karl, T.; Hansel, A.; Hunter, J. F.; Cross, E. S.; Kroll, J. H.; Peng, Z., Brune, W. H.; and Jimenez, J. L. *Atm. Chem. Phys.* **2016**, 16:2943-2970

Chapter 2: Comparative evaluation of iron leach from different sources of fly ash under atmospherically relevant conditions

Abstract

Fly ash, an iron-containing byproduct of coal-fired power plants, has been observed in atmospheric aerosol plumes. Under the acidic atmospheric conditions resulting from the uptake of atmospheric gases, iron leached from fly ash can impact global biogeochemical cycles. However, the fly ash source region, as well as its generating power plant, plays an important role in the amount, speciation, and lability of iron. Yet, no comparative studies have been made on iron leached from fly ash from different sources. This study reports the iron mobilization by proton-promoted dissolution from well-characterized fly ash samples from three distinctive locations: U.S. Midwest, Northeast India, and European ash. In addition, the pH dependency of the iron leach rate was investigated. Proton-promoted dissolution showed a variability between source regions with a relative iron leach in order of U.S. Midwest > Northeast India > European ash. In addition, the initial rate of iron leach suggests that source region is indeed a determining factor in the iron leach capacity of fly ash, as dissolution from Midwestern fly ash is also faster than both European and Indian ash. Finally, the combustion process that produces the fly ash has appears to be significant for the iron speciation, given that well-combusted fly ash samples leached mostly Fe^{3+} rather than bioavailable Fe^{2+}. The role of fly ash should therefore be taken into account in order to better understand the effects of combustion particles in atmospheric iron deposition.

Introduction

Fly ash is an atmospheric aerosol produced as a byproduct of coal combustion. As a result of industrialization over the last few decades, the global production of fly ash has risen.[1] In the early 1990s, fly ash production was estimated at over 300 Tg per year worldwide.[2] Recent estimates indicate that the yearly production of fly ash is around 66 Tg in the United States, 90 Tg in China and India each, and over 31 Tg in Europe.[3-6] While efforts have been made to dispose of fly ash and prevent its emission into the atmosphere, field studies performed over the last decade have found fly ash particles in isolated regions of the ocean, suggesting long range atmospheric transport and lifetime.[7-9] All fly ash particles found in the atmosphere are fine particulate matter (<1 μm) released either by direct emission or by fugitive emissions from the handling of fly ash.[10-13] Because of its size and morphology, fly ash tends to have long residence times, long range transport, and high atmospheric lifetimes.[7,8,9] Due to their relatively high iron oxide content, these combustion particles have been suggested to leach iron in to aqueous aerosol droplets, thus producing atmospheric aqueous iron. [13,14] In fact, anthropogenic aerosols, including fly ash, have been shown to contribute approximately 50% of the iron deposited near industrial regions and at least 5% over open oceans.[15]

Iron leach from tropospheric aerosols during atmospheric acidic processing has been suggested as a source of bioavailable Fe(II), in open oceans.[16,17] Fe(II) is a limiting nutrient in isolated regions of the ocean, and deposition of iron has been seen to stimulate phytoplankton growth and promote the sequestration of atmospheric CO_2.[18-21] Thus, the wet deposition of Fe(II) from fly ash may impact climate fluxes.[22,23] Recently, laboratory studies on fly ash standards have shown that anthropogenic combustion aerosols may have a similar stimulatory effect on phytoplankton growth.[13,15,24] Specifically, Chen et al. have shown that fly ash standards leach iron

ions under atmospherically relevant conditions.[13, 25] These studies observed the leach of both Fe(II) and Fe(III) from fly ash, indicating that fly ash may contribute a significant fraction of iron to the atmosphere. [13, 24, 25] However, the availability of iron from fly ash depends closely on its minerology and particle size.[26] Moreover, fly ash chemical composition and particle morphology varies with the source region and combustion process employed. The mineralogy and particle size of fly ash is determined by the chemical composition of the coal employed in the power plant, as well as the combustion process parameters in the boiler, such as air supply, heat of the combustion, and the duration of the combustion.[27] Therefore, coal-fired power plants using coal extracted from different sources may produce fly ash particles with distinctive physicochemical properties and various environmental implications. Yet, prior to this work there was no comparative study on the leach and rate of dissolution of iron from fly ash from different source region.

In this work, we investigated the initial leach rate and yield of Fe(II) and Fe(III) from fly ash samples from three different source regions: United States, India, and Europe. The significant difference in location ensured a different coal and thermal power-plant boiler, providing a comparative element to this study. This study investigated the leach of iron from fly ash at pH 1 and pH 2, acidic conditions that simulate a deliquescent layer of aerosol particles upon the uptake of acidic atmospheric gases.

Experimental Methods

Source Materials

Three fly ash (FA) samples were obtained from coal-fired power plants located in different regions: United States of America (USFA) from the Midwest region, Indian fly ash (INFA) from Northeastern India, and European fly ash (EUFA) from a commercially available standard of fly ash (BCR®-176R) obtained from the European Commission. All reagents employed for sample

characterization and/or dissolution experiments were analytical grade. All reagents were used without further purification.

Morphology and spectroscopy of fly ash

The morphology and bulk composition of the FA samples were investigated using a JEOL 6480LV scanning electron microscopy coupled with energy dispersive X-ray analysis (SEM-EDX). The size distribution of the fly ash particles was determined by measuring the diameters of randomized fly ash samples. In addition, surface areas for all dust samples were determined using an eleven-point N_2-BET adsorption isotherm that was acquired with a Quantachrome Nova 1200 surface area analyzer. To prepare the samples for BET analysis, the samples were degassed overnight at 300 ˚C.

Bulk elemental composition analysis of FA particles was measured using a Bruker Tracer III SD X-ray fluorescence spectroscopy (XRF). In addition, total iron content of all three FA samples was measured via Atomic Absorption Spectroscopy (AAS) using a PerkinElmer AAnalyst 800 spectrometer. Approximately 0.1 g of fly ash samples were acid digested in Teflon vessels using a mixture of 5 mL HNO_3 and 3 mL H_2O_2. The vessels were tightly sealed and microwaved in an ETHOS microwave digestion system for a two-stage digestion method as described by Iwashita et al.[28]

Total attenuated reflectance infrared spectra (ATR-FTIR) of all fly ash samples were recorded with a single beam Perkin-Elmer FTIR spectrometer, equipped with a ZnSe ATR element and a DLaTGS/KBr detector. Typically 400 scans were acquired at an instrument resolution of 4 cm^{-1} over the full spectral range extending from 800 to 4000 cm^{-1}. Prior to FTIR analysis, all fly ash samples were vacuum dried overnight at 373 K.

Iron leach experiments

Dissolution of iron species from fly ash were performed on a fly ash suspensions of 1 g L^{-1} under atmospherically relevant simulated conditions.[29] Isothermal iron leach experiments were performed in a jacketed glass beaker at 298 K with constantly stirred solutions acidified with hydrochloric acid to a controlled pH set to 1.0 ± 0.1 or 2.0 ± 0.1. Note, Fe^{3+} shows low solubility above pH 3.6.[30] Given the solubility product of concentrations above 60 ppm, a concentration relevant for our iron leach experiments, Fe^{3+} begins to precipitate as $Fe(OH)_3$ above pH 2.4. In fact, increases in pH above this threshold of 2.4 have shown ferric iron precipitation in aqueous solutions with concentrations of Fe^{3+} around 60 ppm. [31] Thus, an upper pH limit of 2.0 ± 0.1 allows for the measurement of Fe^{3+} in solution without hydrolysis loss of iron.[25]

Even though the rate of ferrous iron oxidation is slow, its dependency on pH can lead to oxygenation of Fe^{2+}, particularly as the pH increases.[32] Thus, in order to prevent oxidation of Fe^{2+} once leached from fly ash, all dissolution experiments were carried out under a constant nitrogen purge to prevent oxidation by dissolved oxygen. This oxygen-free environment allowed for a better quantification of both Fe^{3+} and Fe^{2+} leached from fly ash samples during the suspension experiments. In addition, to control the variations in ion strength in the suspension solution as the dissolution of fly ash particles takes place, all acidic solutions were adjusted to an activity of 1 N NaCl.

Kinetic measurements started at a t = 0 minutes, defined as the moment of fly ash loading into the solution. After t = 0 minutes, aliquots of the suspension were taken periodically, filtered with a 0.2 μm filter, and colorimetrically analyzed for dissolved iron content.[33] Dissolved iron speciation was quantified using 1,10-phenanthroline, which forms an orange complex with Fe^{2+} with an absorbance band at 510 nm. Total dissolved iron was quantified in the same samples by

adding hydroxylamine to reduce all Fe^{3+} to Fe^{2+} prior to phenanthroline complexation. All colorimetric complexes were measured in a Lambda 35 Perkin-Elmer UV/Vis spectrophotometer.

Findings of the study

Morphological study of fly ash samples

Particle size and morphology has been shown to have important implications in the leach of iron from aerosol particles. In general, as particles become smaller, a greater proportion of their surface is in physical contact with the acid media and, consequently, available for dissolution.[34] In addition, surface defects and porosity can increase acid media contact area, potentially increasing the initial rate and yield of particle dissolution. In particular, the predominantly spherical particles composing fly ash, which are the result of a controlled combustion process characteristic of high-efficiency power plants, offer a relatively large surface-proton contact area. As particles become less spherical, their exposed surface area decreases and its surface-proton contact area drops; nevertheless, as more defects are present in the particles, the surface-acid contact area increases. Therefore, in order to better understand the iron leach from the dissolution of the fly ash particles, the specific surface area and particle size was investigated.

Specific surface areas, S_{BET}, of the three fly ash samples examined are (1.8±0.1) m^2g^{-1}, (0.98±0.03) m^2g^{-1} and (2.8±0.1) m^2g^{-1} for USFA, INFA and EUFA, respectively. Most particles examined in the fly ash samples were spherical in shape; however, EUFA showed a high proportion of irregular shaped particles. The relatively high fraction of non-spherical particles found in EUFA suggests an incomplete combustion process, as a higher fraction of spherical particles is an indication of a thorough combustion process.[13] In general, particles are observed to aggregate, with clusters of smaller particles attached onto larger ones, as seen in the micrograph for the fly ash samples investigated in Figure 2.1. Overall, the specific surface area indicates that

EUFA will have a larger area exposed to the acidic media, while INFA will have less area in contact with the aqueous phase.

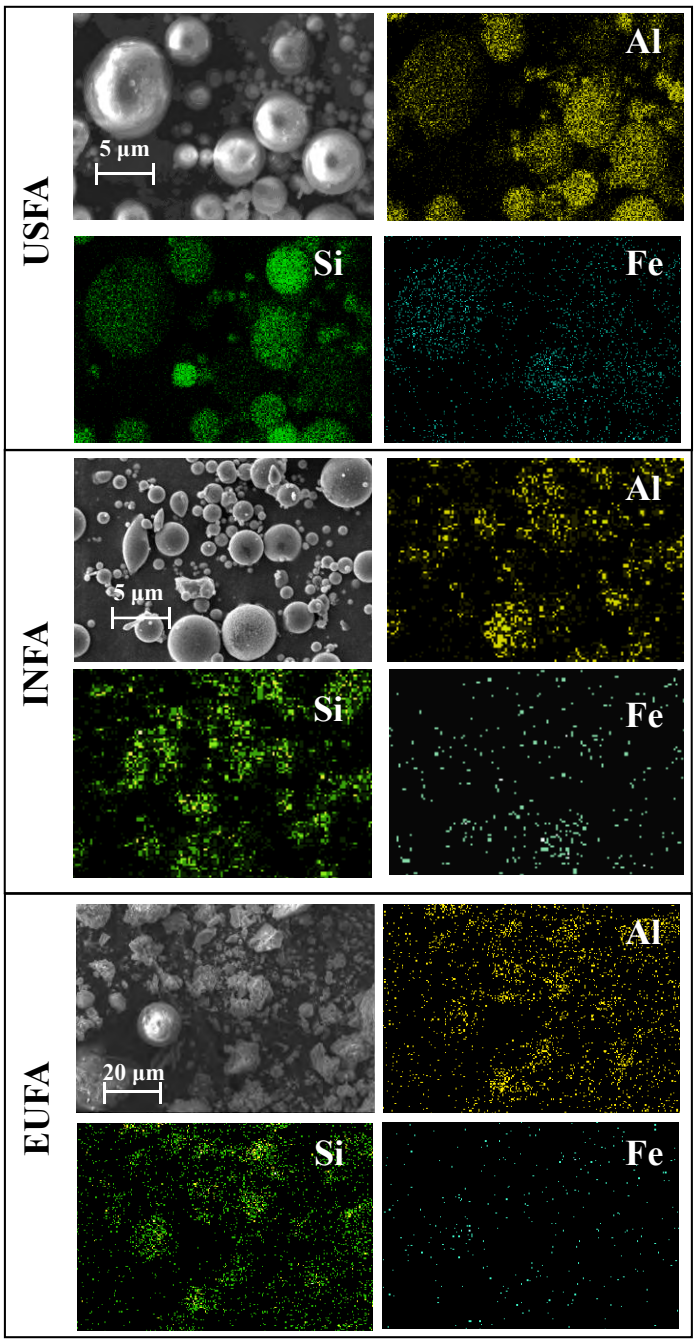

Figure 2.1. Representative micrographs and corresponding Al, Si, and Fe elemental maps obtained from SEM/EDX analysis of fly ash samples.

Each micrograph shown in Figure 2.1 has an elemental mapping that corresponds to the same micrograph, which shows that particles have a homogeneous distribution of minerals containing aluminum, silicon and iron in the spherical particles. However, the elemental composition of individual particle is different, leading to a heterogeneous distribution of metal oxides in each sample.[13]

Figure 2.2 shows the size distribution of fly ash particles examined. All size distributions consider only spherically shaped particles, even in EUFA, which has significant irregular shaped particles. In general, spherical particles show a good fitting to a LogNormal size distribution,[35] as described by equation 1.1:

$$\left(\frac{dn}{d(d)}\right) = \left(\frac{dn}{d(d)}\right)_0 + \frac{A}{dw\sqrt{2\pi}} e^{\frac{-\left[Ln\frac{d}{\bar{d}}\right]^2}{2w^2}} \tag{2.1}$$

where n is the number of particles, $\left(\frac{dn}{d(d)}\right)$ is the normalized particle diameter, A and w are the amplitude and width of the normal distribution, d is the particle diameter and $\bar{d}$ is the arithmetic mean of the particle diameter. For each sample examined, $\bar{d}$ was determined from a sample of at least 350 particle count, yielding values of (1.59±0.05) μm, (2.07±0.04) μm, and (4.6±0.2) μm for USFA, INFA, and EUFA, respectively. The modal diameter, d_m, corresponds to the maxima in the LogNormal fitting shown in Figure 2.2, and it represents the most probable particle diameter in each sample. The d_m was determined from the optimization of the LogNormal particle size distribution, the first order derivative of equation (2.1):

$$\frac{d\left(\frac{dn}{d(d)}\right)}{dd} = 0 \Rightarrow d_m = \bar{d}e^{w^2} \tag{2.2}$$

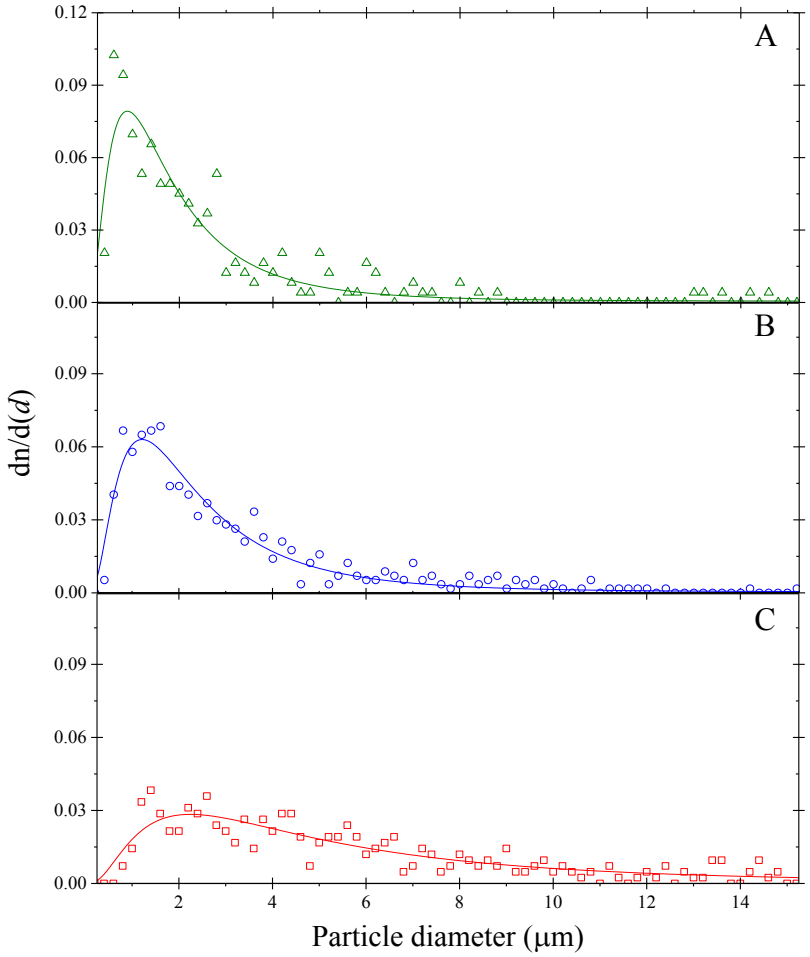

Figure 2.2. Lognormal size distribution of (A) American Midwestern fly ash (USFA); (B) Northeast India (INFA); and (C) European fly ash (EUFA). Histograms are the result of random micrograph and at least 350 particles measured.

As expected, the maxima in the LogNormal modal, suggests that the distribution diameters yields values below the arithmetic mean: (0.89±0.08) μm, (1.21±0.06) μm, and (2.2±0.3) μm for USFA, INFA, and EUFA, respectively. Thus, fly ash samples examined in this work have a higher density of particles with a significantly smaller particle diameter than the median particle diameter; in fact, the higher proportion of particles represented as the maxima in the plots in Figure 2.2 are around 50% smaller that the particle size median. The probability for smaller particles in the fly ash samples, as suggested by modal diameters, can have important implications on the degree of

iron leach upon acidic processing. A greater abundance of smaller particles may lead to enhancements in particle dissolution and iron leach, since the available surface-acid interface that leads to the metal leach is inherently larger in smaller particles.[36, 36, 37] In addition, particle defects and porosity will tend to increase the surface reaction with H^+ ions during the particle acidic processing, which can play an important role in iron solubility.[34]

An evaluation of the available surface with respect to the sphericity of the particles, ψ, allows for a comparative assessment of the surface defect of the particles and the combustion process that produced the fly ash samples. The sphericity, as proposed by Wadell,[38] was estimated as the ratio of the arithmetic mean of the particles, $\bar{d}$, to the geometric diameter of a perfect sphere calculated from the specific surface areas determined through BET, d_{BET}:

$$\psi = \frac{\bar{d}}{d_{BET}} \Rightarrow \psi = \frac{\pi \bar{d}^2}{S_{BET}} \tag{2.3}$$

For the purpose of this study, ψ values lower than 1 are a good indicator of high surface defects and porosity rather than just particle shape. Indeed, given the defects observed through micrographs, all ψ values are significantly lower than 1. USFA and INFA were found to have sphericity values of $(2.1\pm0.1)\times10^{-6}$ and $(3.7\pm0.1)\times10^{-6}$, indicating that USFA has larger surface defects, allowing for a larger physical contact between the particle surface and the acid media. On the other hand, the ψ ratio for EUFA was found $(4.9\pm0.3)\times10^{-6}$. For USFA and INFA samples, where the particles are mostly spherical in shape, as shown in the representative micrographs shown in Figure 2.1, the low ψ values are an indication of surface defects and porosity. Moreover EUFA has a smaller specific surface area than suggested by the spherical particles alone due to an inefficient combustion compared to that of USFA and INFA. Table 2.1 summarizes the morphological parameters in all fly ash samples.

Table 2.1. Morphology summary of fly ash samples: United States fly ash (USFA), Northeast India fly ash (INFA), and European fly ash (EUFA).

	Mean diameter, $\bar{d}$ (µm)	**Most probable diameter, d_m (µm)**	**BET surface area, S_{BET} (m^2g^{-1})**	**Sphericity, $\psi \times 10^{-6}$**	**Observation**
USFA	1.59±0.05	0.89±0.08	1.8±0.1	2.1±0.1	Larger surface area due to smaller particle size
INFA	2.07±0.04	1.21±0.06	0.98±0.03	3.7±0.1	Smaller surface area due to larger particle size
EUFA	4.6±0.2[1]	2.2±0.3[1]	2.8±0.1	4.9±0.3	Smaller fraction of spherical particles due to incomplete combustion. Highest surface area due to surface defects.

[1] Value obtained from spherical particles only

The incomplete combustion of EUFA suggests an iron speciation with a higher proportion of Fe^{2+} relative to that in USFA and INFA, since an inefficient combustion will not completely oxidize all Fe^{2+} contained in coal samples.[15] While the physical contact between particle surface and the acid media suggests a greater surface-proton interaction for USFA, where the largest deviation from spherical surface is observed, the chemical composition of the particles indicate the effectiveness of the surface-proton interaction towards particle dissolution.

ATR-FTIR spectroscopy of fly ash samples

The exposed surface available for dissolution will interact with protons and aqueous phase as a function of its chemical composition and affinity towards water and acidic media. A sample with higher affinity towards dissolution will lead to higher iron dissolution rates.[34] ATR-FTIR spectroscopy provides insight into the composition and chemical properties of the ash samples. The spectra of the dried fly ash samples are shown in Figure 2.3. The upper panel in Figure 2.3 shows the entire region from 700 cm^{-1} to 4000 cm^{-1}, with an insert showing an expansion region from 2750 cm^{-1} to 3800 cm^{-1} whereas the lower panel shows a magnified view of the region from

700 cm^{-1} to 1750 cm^{-1}. Based on previous literature assignments, the vibrational absorption bands are assigned to fundamental vibrational modes in Table 2.2.

The insert shows a band centered around 3673 cm^{-1} for both Indian and European fly ash, assigned to the ν (OH) of structural hydroxyl groups. These spectral features suggest that both EUFA and INFA have the potential for formation of relatively more hydrogen bonds in surfaces than that on USFA. In addition, EUFA shows additional inner structural hydroxyl bands in the region of 3600 cm^{-1}, not observed in either USFA or INFA. In particular, EUFA shows a broad band attributed to the hydrogen bonding stretching region around 3455 cm^{-1} due to the presence of water. This observation indicates that the mineralogy of EUFA contains non-combusted particles with more interlayers capable to adsorb water and interact with H^+ ions in the acidic solutions.[39, 40]

In the lower panel of Figure 2.3, European fly ash shows absorption bands in the 140 cm^{-1} region, assigned to the bending mode of carbonates. In addition, a EUFA shows a characteristic band at 1628 cm^{-1} due to the stretching vibration of –COO– of bicarbonates.[41] These carbonate and bicarbonate spectral features are absent in both United States and Indian fly ashes, indicating the relatively poor combustion of EUFA, as suggested by the higher presence of non-spherical particles seen in the micrographs shown in Figure 2.1.

All fly ash samples show bands in the spectral region from 900 and 1700 cm^{-1}, assigned to vibrational absorptions bands due to lattice stretching motions of Si-O. The lower panel in Figure 2.3 shows differences in frequency and peak intensities over this region for the three fly ash samples. In particular, both USFA and EUFA show ν(Si-O) centered at 931 cm^{-1} to 1100 cm^{-1}, contrasting with the same bands displayed at around 1037 cm^{-1} and 1152 cm^{-1} for INFA. This difference can be attributed to the lattice structures. In addition, bands near 780 cm^{-1} were assigned

to deformation modes of Fe^{3+} and alkaline earth, δ (FeCa-OH).[42] The bands around 875 cm^{-1} for were also deformation modes of Fe^{3+} associated with aluminum, δ (FeAl-OH).

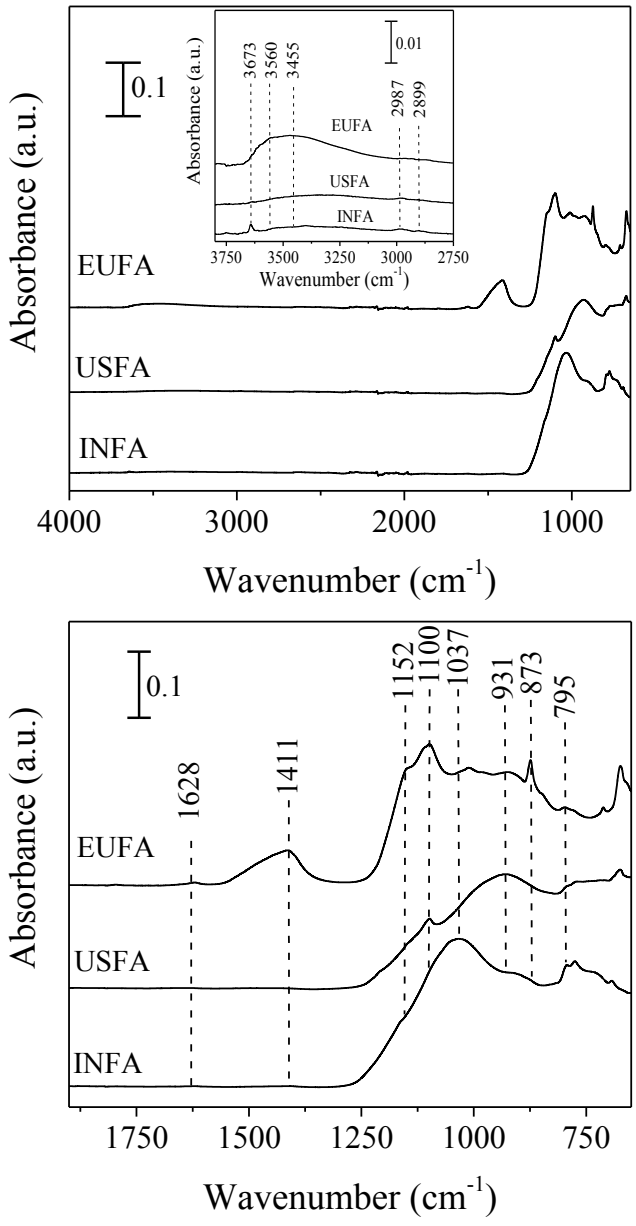

Figure 2.3. Top panel: Attenuated total reflection–Fourier transform infrared (ATR-FTIR) spectra showing all three authentic fly ashes: United States fly ash (USFA), Northeast India fly ash (INFA), and European fly ash (EUFA). The inset shows a magnified view of the spectral region from 2750 to 3800 cm^{-1}. Lower panel: spectral region from 650 to 1850 cm^{-1}.

Table 2.2. The peak assignments for the vibrational modes of fly ash as detected using ATR-FTIR.

Vibration Assignment and Mode Description	**USFA**	**INFA**	**EUFA**	**Literature**
δ(FeCa-OH)	795, 771	777	795	785 [41]
δ(AlFe-OH)	-	-	873	873, [43] 885 [44]
δ(AlAl-OH)	925	914	915	916, [44] 920 [43]
ν(Si-O)	989	1006	-	992, [44], 995, [43]
ν(Si-O)	1001	1037	1012	1008, [43] 1060 [43], 1027 [44]
ν(Si-O)	1100	1152	1100	1116, [44] 1102 [44]
$\nu_3(CO_3^{2-})$	n.o.	n.o.	1411	1410 [44]
$\nu_4(CO_3^{2-})$	n.o.	n.o.	1450	1430 [44, 43]
$\nu(HCO_3^-)$	n.o.	n.o.	1628	1630-1620 [41]
ν(OH) structural hydroxyl	n.o.	3673	n.o	3626, [43] 3642 [45], 3698 [44]
Vibrational frequencies in cm^{-1}.				

All fly ash samples showed iron content associated with alkaline earth and/or aluminum elements. Finally, spectra for all three samples showed δ (AlAl-OH) at 930 cm^{-1}. Overall, the ATR-FTIR spectra showed that all three fly ash samples were abundant in Al and Si, with some amount of Fe. Moreover, the ATR-FTIR bands suggested a higher content of Fe^{3+}, an oxidation state consistent with the combustion process that generated fly ash.[40] Thus, iron leach from fly ash particles was expected to be larger in Fe^{3+}. In addition, spectral features suggest that all fly ash samples have exposed edge sites with Al-OH and Si-OH bond terminals,[46] which was consistent with literature reports of silica and mullite ($3Al_2O_3 \cdot 2SiO_2$) content in fly ash.[47] The formation of mullite and silica in fly ash has been suggested to follow a two-step mechanism during the

combustion process, where kaolinite ($Al_2O_3 \cdot 2SiO_2 \cdot 2H_2O$) forms metakalin ($Al_2O_3 \cdot 2SiO_2$), and further combustion leads to mullite:

$$Al_2O_3 \cdot 2SiO_2 \cdot 2H_2O(s) \longrightarrow Al_2O_3 \cdot 2SiO_2(s) + 2H_2O(g) \quad (1.4)$$

$$3(Al_2O_3 \cdot 2SiO_2)(s) \longrightarrow 3Al_2O_3 \cdot 2SiO_2(s) + 4SiO_2(2) \quad (1.5)$$

where the loss of the well crystallized alumminosilicate clay minerals leading to mullite and silica has been suggested to decrease the stability of the mineral, which can lead to faster dissolution rates in an acidic media.[13] Overall, the differences between ART-FTIR spectra are a reflection of the variations in mineralogy due to the difference in the power plant efficiency and its coal source.

Elemental composition

X-ray fluorescence spectroscopy (XRF) shows a relative higher bulk content of iron than any other trace element. Table 2.3 summarizes the bulk elemental composition of trace elements in all three fly ash samples, normalized without Al or Si. The difference in trace elemental composition in the bulk can be attributed to differences in the coal mineralogy for the different regions.

In general, the relative content of iron, with respect of other trace elements, was found to be lower in European fly ash, while the largest is found in Indian fly ash. In fact, other than Al, Si, and Fe, INFA has less than 5% of all other trace elements. On the other hand, both USFA and EUFA show a relatively higher content of Ca, with a higher content of Zn in EUFA.

Table 2.3. XRF elemental percentage of the major crustal elements in fly ash samples. The elemental analysis omits major components Al and Si. Error represents the standard deviation over triplicate measurements

	%Fe	%Ca	%Zn	%Ti	%Sr
USFA	40±1	35.8±0.2	1.0±0.1	3.6±0.1	10.5±0.4
INFA	74±3	4.3±0.1	1.0±0.1	5.0±0.1	2±2
EUFA	11.6±0.6	29±1	28±1	3.7±0.2	1.7±0.1

When analyzed using AAS, the content of total iron was found to be 38±2 mg g^{-1}, 25±3 mg g^{-1}, and 9.4±0.8 mg g^{-1}, for USFA, INFA, and EUFA, respectively. The higher amount of iron in USFA indicates that INFA has a relatively smaller proportion of trace elements relative to USFA. Thus, INFA has a relatively significant fraction of aluminosilicates in its bulk composition, where Al and Si are outside the XRF detection range and not shown in Table 2.3. Overall, atomic spectroscopy indicates that the largest amount of iron is found in United States fly ash, while European ash has the lowest content of iron.

Iron leach experiment

Fly ash samples were allowed to dissolve in an acidic suspension, and periodically extracted aliquots were analyzed colorimetrically for Fe^{2+} and Fe^{3+}. Figure 2.4 shows the dissolution speciation of iron as a function of suspension time for the three different ashes examined at pH = 1.0±0.1. An increase in the concentration of both Fe^{2+} and Fe^{3+} was observed in all acid solutions. For the suspensions of USFA and INFA, the amount of Fe^{3+} in solution was higher than Fe^{2+} at any point of the dissolution experiment, as can be seen in the panels *a* and *b* of Figure 2.4.

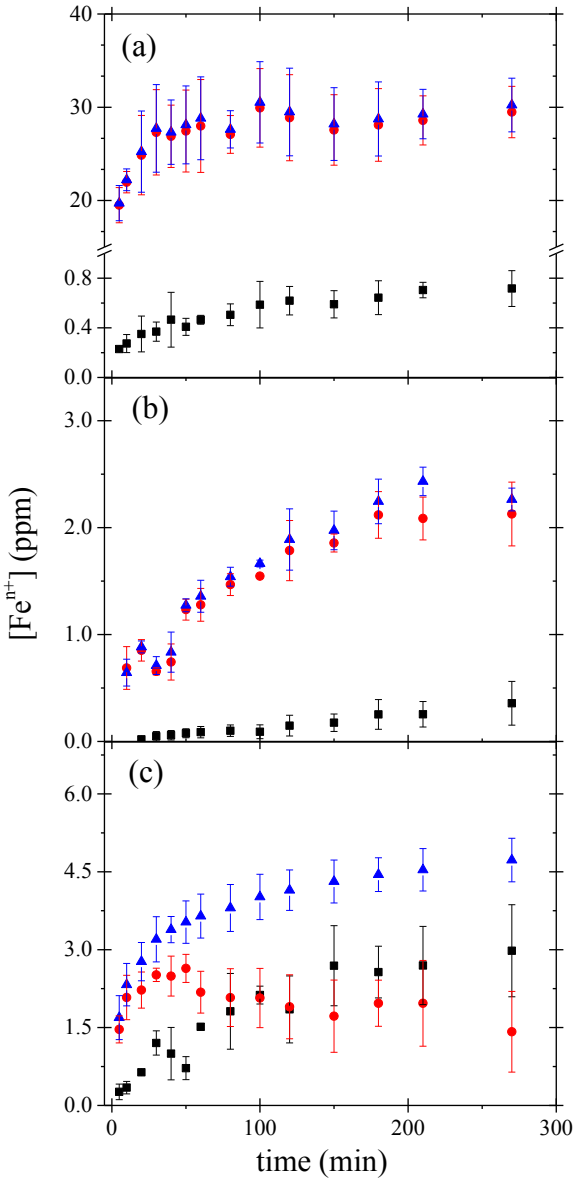

Figure 2.4. Iron dissolution of 1.0 g L^{-1} of fly ash samples in acidified 1.0 M NaCl solutions at pH 1 as a function of time. ■ represents Fe^{2+}, ● represents Fe^{3+}, and ▲ represents total iron. Measured dissolved iron in (a) USFA (b) INFA, and (c) EUFA shows total dissolved iron, dissolved iron (II) and dissolved iron (III) for each sample. Error bars represent one standard deviation from triplicate experiments.

For comparison purposes, Table 2.4 summarizes the iron speciation in the leach experiments at two different reference points: at 500 minutes of fly ash suspension in the acidic media, $[Fe^{n+}]_{500}$, and at 24 hours of suspension, $[Fe^{n+}]_{24}$. This finding supports the observation that Fe^{3+} is the dominant form of iron in fly ash, as a combustion process will favor the formation

of Fe(III) oxide over Fe(II) species. [48] The relatively higher amount of Fe(III) oxides have been explained as the result of the complete combustion of pyrite ($Fe_{5/4}S$) and magnetite (Fe_3O_4), common components of coal, through the following suggested two-step mechanism: [49]

$$\frac{4}{5}Fe_{5/4}S(s) + \frac{28}{15}O_2(g) \xrightarrow[\Delta]{} \frac{1}{3}Fe_3O_4(s) + \frac{4}{5}SO_2(g) \quad (2.6)$$

$$Fe_3O_4(s) + \frac{1}{4}O_2(g) \xrightarrow[\Delta]{} \frac{3}{2}Fe_2O_3(s) \quad (2.7)$$

Indeed, after 500 minutes of suspension, the concentration of Fe^{3+} in solution leached from USFA was nearly 31 times larger than that of Fe^{2+}, while INFA only showed detectable Fe^{3+} in solution. Leach of Fe^{2+} from INFA suspension was only detectable after 700 minutes; before that time, the concentration of Fe^{2+} in solution was below 30 ppb, the limit of detection of the colorimetric method. In contrast, the suspension of EUFA in a pH 1 solution showed statistically similar concentrations of Fe^{3+} and Fe^{2+} between 80 minutes and 24 hours of reaction. As reported in Table 2.4, after 24 hours of EUFA suspension, the amount of Fe^{2+} leached in to solution becomes higher than the amount found of Fe^{3+} in solution. This supports the observation of an incomplete combustion of coal in the formation of the EUFA sample, as suggested by the micrographs and FTIR analysis (*vide supra*). The iron speciation in the solution phase in the EUFA suspension was the result of dissolution of iron-containing minerals in non-combusted coal particles, as well as the dissolution of both Fe^{3+} and Fe^{2+} in the partially combusted particles.

After a complete combustion process, the iron leach should yield Fe^{3+} only. However, the presence of both Fe^{3+} and Fe^{2+} in all fly ash suspension experiments was the product of iron oxides contained in magnetite, a common component in partially combusted coal as shown in equation (2.6), which can leach Fe^{2+}:[48]

$$\frac{1}{2}Fe_2O_3(s) + 3H^+(aq) \longrightarrow Fe^{3+}(aq) + \frac{3}{2}H_2O(l) \quad (2.8)$$

$$FeO(s) + 2H^+(aq) \longrightarrow Fe^{2+}(aq) + H_2O(l) \quad (2.9)$$

Figure 2.4 suggests that iron dissolution from the fly ash samples examined was faster in USFA than in the other samples. Overall, the proton promoted iron leach from fly ash suspensions exhibit two pathways: an initial, rapid iron leach upon fly ash introduction into the pH 1 solution, followed by a slower leach of iron. The fast iron leach occurred on a time scale faster than our experimental resolution and it was clearly observed in USFA and EUFA leach of total iron, while iron leach from INFA did not show the faster iron dissolution pathway. The rapid dissolution suggested the presence of surface iron species interacting directly with protons through reactions similar to equations (2.8) and (2.9).[50] Based on our experimental resolution, the lower boundary of the initial rate of this rapid total iron (Fe^{3+} + Fe^{2+}) leach, v_f, was estimated to be (3.9±0.4) × 10^{15} molecules cm^{-3} s^{-1} and (3.3±0.8) × 10^{14} molecules cm^{-3} s^{-1} for USFA and EUFA at pH 1, respectively. In addition, iron leaching from fly ash slowly plateaued to a maxima iron leach in all cases. Considering the iron content in each fly ash sample examined, INFA yielded a considerably lower proportion of its iron content at a slower rate. These observations suggest that the mineralogy variations evidenced by the differences in the ATR-FTIR spectral features, a reflection of the coal source and combustion efficiency, play an important role in the leaching of iron.

Table 2.4. Concentration of iron species in solution leached from fly ash at 500 minutes of suspension $[Fe^{n+}]_{500}$, and 24 hours of suspension $[Fe^{n+}]_{24}$. All concentrations were reported in ppm. The errors were the standard deviation over, at least, triplicate experiments.

Sample	Iron concentration (ppm) at pH=1				Iron concentration (ppm) at pH=2			
	$[Fe^{2+}]_{500}$	$[Fe^{3+}]_{500}$	$[Fe^{2+}]_{24}$	$[Fe^{3+}]_{24}$	$[Fe^{2+}]_{500}$	$[Fe^{3+}]_{500}$	$[Fe^{2+}]_{24}$	$[Fe^{3+}]_{24}$
USFA	0.9±0.3	27±3	1.2±0.2	31±1	0.89±0.05	21±5	1.1±0.1	25.2±0.5
INFA	0.6±0.3	2.7±0.5	0.8±0.4	6±3	0. 3±0.2	1.46±0.02	1.2±0.4	2.6±0.8
EUFA	3.2±0.6	1.8±0.8	4.4±0.1	2.0±0.6	1.2±0.4	1.6±0.1	2.2±0.1	1.8±0.8

The initial, fast leach of iron was followed by a slower leach attributed to the proton promoted dissolution taking place as the result of H^+ ions interacting with particle surface functional groups, such as hydroxyl terminals and, in the case of the incomplete combustion particles found in EUFA, carbonates and hydroxyl groups. [51]As the proton complexes with the fly ash surface, it freed additional iron oxides or iron-containing incompletely combusted particles to continue the dissolution process. [13] The initial rate of the slower proton promoted leach of iron, v_s, and the fast pathway, v_f, is summarized in Table 2.5. The slow pathway of USFA is relatively faster than that in INFA, which mirrors the initial rate sequence observed for the fast pathway. All initial rates for the slow pathway were determined from the slopes of the initial linear segment of the leach rate plot shown in Figure 2.4, the data between minute 5 (first data point) up to the loss in linearity. The limit of linearity was calculated with a 95% of confidence in each case.[52] It can be observed in Table 2.5 that the leach of Fe^{2+} was slower than that of Fe^{3+}. The observed initial rate of the slow pathway, v_s, for each iron species have a different dependency on the pH:

$$v_s = \frac{d[Fe^{n+}_{(aq)}]}{dt} = k[H^+]^m[Fe^{n+}_{FA}] \tag{2.10}$$

where Fe_{FA}^{n+} is the iron available in fly ash present in the surface and the bulk, n = 2 or 3 and m is iron leach reaction order. Given the stoichiometric coefficients in equations (2.8) and (2.9), the initial rate of Fe^{3+} leach from the oxide particles primarily present in USFA and INFA was more prone to changes in pH than that of Fe^{2+} leach. Thus, since the pH was constant throughout the experiment, the initial rate of the second (slow) pathway, v_s was faster for the leach of Fe^{3+}, as indicated in the data summarized in Table 2.5. In addition, ferrous iron present is mostly found in the bulk of the particle rather than the surface. This suggests that, as the particle progressively dissolves and breaks down in the acidic solution, a higher fraction of Fe^{2+} species becomes available for acidic processing.[13] As a consequence, the dissolution initial rate of Fe^{2+} is dependent on the rate of dissolution of the surface ferric iron.

The amount of Fe^{2+} leached from the EUFA suspension was the highest from the three samples examined. This observation is consistent the characterization of EUFA particles, which showed an important fraction of non-combusted or partially combusted particles. Iron in non-combusted particles may have been present as part of the crystallized aluminosilicate composition, while partially combusted particles have been suggested to have important magnetite (Fe_3O_4) fraction, as shown in equation (2.6).[49] In all these cases, the composition of the sample includes Fe^{2+}. Because the content of iron in EUFA was not necessarily in an oxide form, the initial rate was the result of a combination of equation (2.10) and the leach of iron content in non-combusted particles. Contrary to the leach of Fe^{3+} in the EUFA suspension, the leach of Fe^{2+} did not undergo the fast pathway observed in USFA, suggesting that the dissolution of Fe^{2+} from EUFA samples was the result of bulk Fe^{2+} rather than surface iron. This observation suggests that Fe^{2+} was mostly contained in unburned minerals, as the combustion process did not consume the framework of the well crystallized aluminosilicate to expose Fe^{2+}. Since the crystal aluminosilicate provides stability

to the particles, no rapid dissolution of Fe^{2+} was available. Overall, the initial slow rate of iron leach from EUFA suspension was slower than that from USFA, as summarized in Table 2.5.

Table 2.5. Initial rate of the fast (v_f) and slow (v_s) dissolution pathways of iron species leached from fly ash. The errors are the standard deviation over, at least, triplicate experiments.

pH	Sample	v_f (×10^{15} molec. cm^{-3} s^{-1})			v_s (×10^{13} molec. cm^{-3} s^{-1})		
		Fe^{2+}	Fe^{3+}	Total Fe	Fe^{2+}	Fe^{3+}	Total Fe
1	USFA	0.045±0.004	3.8±0.4	3.9±0.4	0.062±0.006	3.4±0.8	3.5±0.8
	INFA	n.o.	n.o.	n.o.	0.039±0.002	0.21±0.09	0.24±0.09
	EUFA	0.05±0.03	0.29±0.05	0.33±0.08	0.38±0.05	0.43±0.01	0.7 ±0.1
2	USFA	n.o.	0.42±0.05	042±0.05	0.065±0.006	4.3±0.5	4.4±0.6
	INFA	n.o.	n.o.	n.o.	0.021±0.002	0.18±0.02	0.20±0.02
	EUFA	n.o.	n.o.	n.o.	0.18±0.05	0.22±0.02	0.33±0.02

n.o.: Not observed

Figure 2.5 shows the dissolution speciation of iron for the three different fly ash samples examined at pH = 2.0±0.1. As observed in pH 1 suspensions, an increase in the concentration of both iron species was observed throughout the experiment time. Overall, as expected from equation (8) and (9), the leach of iron slows down for all samples with the decrease in concentration of H^+ ions. In fact, the fast leach pathway observed in the pH 1 suspension of USFA and EUFA decreases substantially as the pH increases. In the case of USFA the fast pathway was only observed in the leach of Fe^{3+}, while the fast pathway in EUFA was completely suppressed at pH 2. The fast initial rate of the total iron leach from USFA decreased from (3.9±0.4) × 10^{15} molec. cm^{-3} s^{-1} at pH 1 to (4.2±0.5) × 10^{14} molec. cm^{-3} s^{-1} at pH 2, a drop of approximately 90%. Table

2.5 summarizes the initial rate for both the slower proton promoted leach of iron, v_s, and the fast pathway, v_f.

In addition, for pH 2 solutions, the initial rate of the slow pathway showed a similar trend to that observed in pH 1 suspensions, with the highest dissolution rate observed in USFA and the slowest in INFA. However, the initial rates observed at pH 2 were lower than those in pH 1 solutions. Table 2.5 summarize the initial rates calculated for both pH 1 and pH 2, respectively. It can be seen that the values of v_s at pH 2 show no statistically significant change for the leach of total iron, Fe(II), and Fe(III) from USFA. On the other hand, v_s for the leach of total iron at pH 2 significantly dropped for the other samples studied, with a decline from pH 1 of 83% and 47% for INFA and EUFA, respectively. In addition, initial rates suggest that the decrease in the slow pathway leach rate of Fe^{3+} depends closely on pH, as the initial rate decrease of Fe^{3+} leach for pH 2 relative to pH 1 was estimated to be 86% and 51% for INFA and EUFA, respectively. Conversely, the initial rate decrease of Fe^{2+} leach is estimated to be 54% and 47% for INFA and EUFA, respectively. In all cases, the concentration of iron slowly plateaued to equilibrium concentrations.

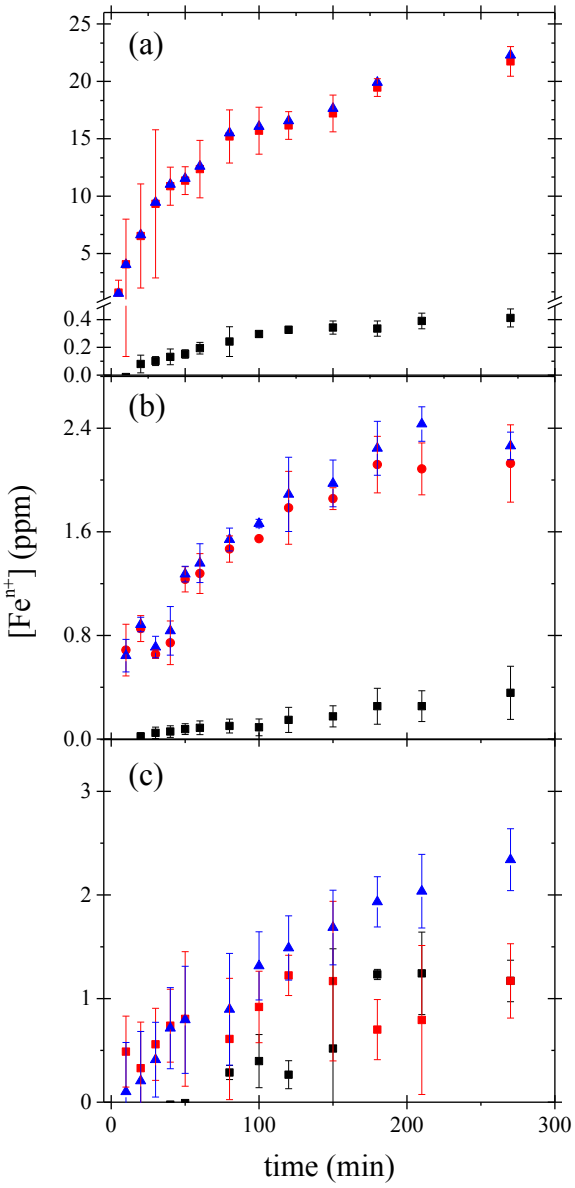

Figure 2.5. Iron dissolution of 1.0 g L^{-1} of fly ash samples in acidified 1.0 M NaCl solutions at pH 2 as a function of time. ■ represents Fe^{2+}, ● represents Fe^{2+}, and ▲ represents total iron. Measured dissolved iron in (a) USFA (b) INFA, and (c) EUFA shows total dissolved iron, dissolved iron (II) and dissolved iron (III) for each sample. Error bars represent one standard deviation from triplicate experiments.

In order to make a direct comparison of the iron leached from each fly ash sample, the concentration of total iron remaining in fly ash at a given suspension time *t* was calculated from the normalized concentration of total iron leached and the iron content in the fly ash loading, as

determined by atomic absorption spectroscopy analysis and the experimental suspended fly ash loading of 1 g L^{-1}:

$$\text{Fraction of iron remaining in fly ash samples} = 1 - \frac{([Fe^{2+}]_t + [Fe^{3+}]_t)}{([Fe^{2+}]_{FA} + [Fe^{3+}]_{FA})} \qquad (2.11)$$

where $[Fe^{n+}]_{FA}$ is the concentration of iron available in fly ash (with n beeing the oxidation state of iron), and $[Fe^{n+}]_t$ represents the concentration of total iron leached at a time *t*. Figure 6 shows the time progression of the fraction of total iron remaining in the fly ash samples. Using equation (2.11), the fraction of total iron leached in USFA was estimated to reach a maximum of around 80 % in the solution phase at pH 1 beyond 500 minutes of suspension. In addition, after 500 minutes the fraction of leached iron at pH 1 and pH 2 are statistically similar. Conversely, the lowest total iron dissolution fraction was observed in INFA suspensions, where the fraction leached at pH 1 was around 10 %. However, in the case of INFA suspensions the fraction of dissolved iron in pH 1 and pH 2 are statistically similar beyond 150 minutes. Finally, EUFA in pH 1 solutions reached a maximum fraction of iron leached at around 150 minutes of suspension, and the fraction of iron leached is statistically higher at pH 1 than at pH 2 until 720 minutes of suspension.

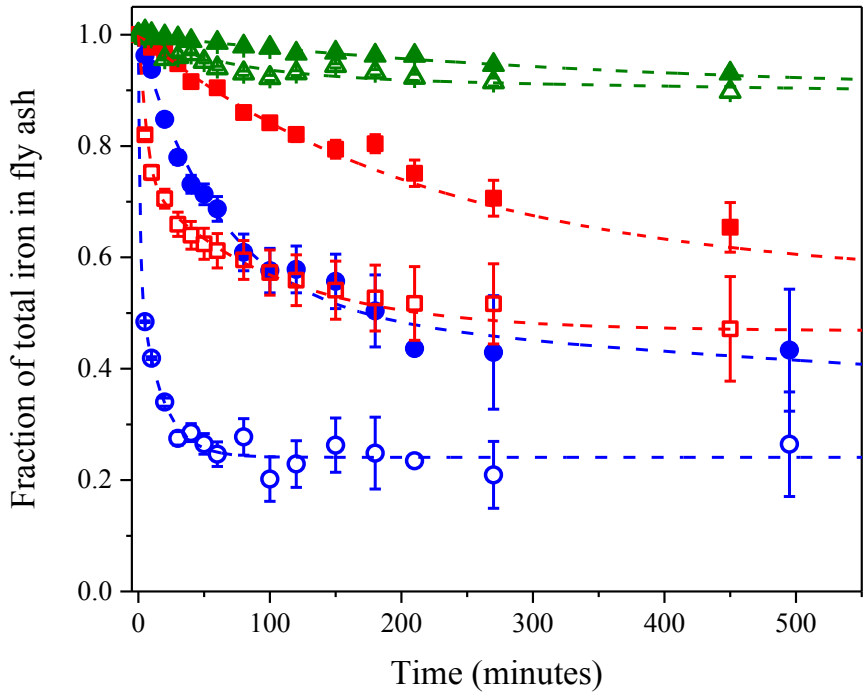

Figure 2.6. Fraction of total iron in fly ash samples. Clear symbols represent the fraction of iron leached from fly ash suspensions in pH 1 solutions; full symbols represent the fraction of iron leached from fly ash suspensions in pH 2 solutions. Blue circles correspond to iron leached from USFA, red squares correspond to iron leached from EUFA, and green triangles represent iron leached from INFA.

Previous dissolution experiments at pH 1 that used fly ash standard materials with higher Fe^{2+} content showed a total iron leached of around 50%.[13, 25] While this observation was consistent with the total iron leach from EUFA, the sample with the largest leach of ferrous ions, our results suggest that particle size and mineralogy, as well as the coal-combustion efficiency, play an important role not only in the solubility of total iron but also in iron speciation in the solution phase. Significantly, USFA, the fly ash sample with the largest relative iron content reported in this work, shows the highest amount of iron solubility at faster rates. In fact, the fast pathway at pH 1 for USFA accounted for over 50% of the total iron leach. On the other hand, the fast pathway at pH 1 for EUFA accounted for around 18% of total iron leached into solution. In addition, as observed in Figures 2.4 and 2.5, only a small fast pathway was observed at pH 2 in USFA, which

accounted for only 2% of the total iron leached. With the exception of EUFA samples, most of the total iron reported in Figure 2.6 corresponded to Fe^{3+}. Finally, Figure 6 shows that pH 1 total iron dissolution was consistently faster than at pH 2, as the fraction of total iron in fly ash plateaued earlier at the lower pH. This observation supported the rate dependency on the concentration of H^+, as expressed in equation (2.10). This result suggests that variability between fly ash source regions have distinctive atmospheric effects.

Atmospheric Implications

Recent field observations suggest that fly ash particles can be considered a source of atmospheric iron.[1, 7, 8, 53] However, most laboratory studies available use fly ash standards, with no distinction between source regions of combustion process. [13, 25] The comparative study we present here shows that the atmospheric acidic processing of three different fly ash samples from three different sources, including United States, India, and Europe, yields significant variations in iron mobilization. The proton-promoted dissolution of iron shows a relative percent of iron leached from each sample are in order of USFA > EUFA > INFA. Compared to mineral dust dissolution, combustion aerosol samples may play a more important role in mobilizing Fe^{3+} than Fe^{2+}. [26, 54] Our study suggest that only partially-combusted or non-well combusted particles will leach bioavailable Fe^{2+} as a result of the deliquescent layer of an aerosol particle upon the uptake of acidic atmospheric gases. Thus, the combustion efficiency of coal-fired power plants play a significant role in the speciation of iron mobilized by atmospheric acidic processing.

Our results also indicate that the impact of pH in the rate of iron dissolution varies significantly with the source region. In particular, USFA shows a two-step pathway of iron leach: the initial rate of iron leached from USFA shows a pH effect only for an initial fast dissolution pathway, there is no statistically significant influence by pH for the slower pathway. Conversely,

samples from India and Europe show mostly a single slow pathway, with a rate that drops when the solution acidity decreases from pH 1 to pH 2. This difference could be due to a high proportion of surface and/or labile iron in USFA compared to that in INFA and EUFA. Nevertheless, changes in the pH continue to show the same proportion of iron speciation, with a significantly higher proportion of acid mobilized Fe^{3+} with respect of Fe^{2+}. In fact, the acidic processing of the fully combusted samples (USFA and INFA) examined in our work show that for USFA 93 % of the iron leached is Fe^{3+}, while for INFA 88 % of the total iron leached is Fe^{3+}. On the basis of these results, it can be proposed that only partially-combusted coal is a significant source of bioavailable iron in the atmosphere. However, in order to better understand the biogeochemical cycle of atmospheric iron, additional reduction mechanisms of iron should be considered.[55, 56]

References

1. Ojha, K.; Pradhan, N. C.; Samanta, A. N. *Bulletin of Materials Science* **2004,** *27* (6), 555-564.
2. Manz, O. E. *Fuel* **1997,** *76* (8), 691-696.
3. *2013 Coal Combustion Product (CCP) Production & Use Survey Report. Aurora, CO: American Coal Ash Association.* (2014).
4. Haque, E. *Int. J. Waste Resou.* **2013,** *3* (1), 22-25.
5. Feuerborn, H. J. *World of Coal Conference*, **2011** Denver, CO,.
6. Cai, X. P.; Zhang, S. Q.; Li, J. G. *Water Res. Environ.* **2015** Beijing,.
7. Ramanathan, V.; Crutzen, P. J.; Kiehl, J. T.; Rosenfeld, D. *Science* **2001,** *294* (5549), 2119-2124.
8. Inoue, J.; Momose, A.; Okudaria, T.; Murakami-Kitase, A.; Yamazaki, H.; Yoshikawa, S. *Atmos. Environ.* **2014,** *95,* 375-382.
9. Feuerborn, H. J.; Momose, A.; Okudaria, T.; Murakamir-Kitase, A.; Yoshikawa, S. *Atmos. Environ.* **2014,** *95,* 375-382.
10. Andreae, M. O.; Crutzen, P. J. *Science* **1997,** *276* (5315), 1052-1058.
11. Li, W.; Shao, L. *J Geophys. Res.: Atmos.* **2009,** *114 (D9)* (D09302), DOI: 10.1029/2008JD011285.
12. Muller, S. F.; Mallard, J. W.; Mao, Q.; Shaw, S. L. *J. Air & Waste Manag. Assoc.* **2013,** *63* (7), 806-818.

13. Chen, H.; Laskin, A.; Baltrusaitis, J.; Gorski, C. A.; Scherer, M. M.; Grassian, V. H. *Environ. Sci. & Tech.* **2012,** *46,* 2112-2120.

14. Kutchko, B. G.; Kim, A. G. *Fuel* **2006,** *85* (17-18), 2537-2544.

15. Luo , C.; Mahowald , N.; Bond, T.; Chuan, P. Y.; Schauer, J. *Global Biogeochemical Cycles* **2008,** *22,* GB1012.

16. Duce, R. A.; Tindale, N. W. *Am. Soc. Limnology and Oceanography* **1991,** *36* (8), 1715-1726.

17. Fan, S.; Moxim, W. J.; Levy, H. *Geophys. Res. Letters* **2006,** *33*.

18. Fung, I. Y.; Meyn, S. K.; Tegen, I.; Doney, S. C.; John, J. G.; Bishop, J. K. B. *Global Biogeochemical Cycles* **2000,** *14* (1), 281-295.

19. Martin, J. H.; Fitzwater, S. E. *Nature* **1988,** *331,* 341-343.

20. Bonnet, S.; Guieu, C. *Geophys. Res. Letters* **2004,** *31*.

21. Boyd, P. W.; Watson, A. J.; Law, C. S.; Abraham, E. R.; Trull, T.; Murdoch, R.; Bakker, D. C. E.; Bowie, A. R.; Buesseler, K. O.; Chang, H.; Charette, M.; Croot, P.; Downing, K.; Frew, R.; Gall, M.; Hadfield, M.; Hall, J.; Harvey, M.; Jameson, G.; LaRoche, J.; Liddicoat, M.; Ling, R.; Maldonado, M. T.; McKay, M. R.; Nodder, S.; Pickmere, S.; Pridmore, R.; Rintoul, S.; Safi, K.; Sutton, P.; Strzepek, R.; Tanneberger, K.; Turner, S.; Waite, A.; Zeldis, J. *Nature* **2000,** *407,* 695-702.

22. Riebesell, U.; Wolf-Gladrow, D. A.; Smetacek, V. *Nature* **1993,** *361,* 249-251.

23. Lal, R. *Sust. Agric. II* **2008,** *363* (1492), 815-830.

24. Desboeufs, K V; Sofitkitis, A.; Losno, R.; Colin, L.; Ausset, P. *Chemosphere* **2005,** *58,* 195-203.

25. Chen, H.; Grassian, V. H. *Environ. Sci. Technol.* **2013,** *47,* 10312−10321.

26. Rubasinghege, G.; Robert, L. W.; Michelle, S. M.; Grassian, V. H. *PNAS* **2010,** *107* (15), 6628–6633.

27. Morawska, L.; Zhang, J. *Chemosphere* **2002,** *49,* 1045-1058.

28. Iwashita, A.; Nakajima, T.; Ohki, F. *Talanta* **2007,** *71,* 251-257.

29. Keene, W. C.; Sander, R.; Pszenny, A. A. P.; Vogt, R.; Crutzen, P. J.; Galloway, J. N. *J. Aer. Sci.* **1998,** *29* (3), 339-356.

30. Seinfeld, J. H.; Pandis , S. N. *Atmospheric Chemistry and Physics: From Air Pollution to Climate Change;* Wiley: Hoboken, N. J., 2006.

31. Harris, D. C. *Exploring chemical analysis,* 2nd ed.; W. H. Freeman and Company: New York, 1997.

32. Stumm, W.; Lee, G. F. *Ind. Eng. Chem.* **1961,** *53* (2), 143–146.

33. Fortune , W. B.; Mellon, M. G. *Ind. Eng. Chem.* **1938,** *10* (2), 60-64.

34. Baker, A. R.; Jickells, T. D. *Geophys. Res. Letters* **2006,** *33* (17), L17608.

35. Heintzenberg, J. Properties of the Log-Normal Particle Size Distribution. *Aer. Sci. Tech.* **2007,** *21* (1), 46-48.

36. Cwiertny, D. ; Baltrusaitis, J.; Hunter , G. ; Laskin, ; Scherer, M. ; Grassian, V. H. *J. Geophys. Res.* **2008,** *113,* D05202.

37. Laskina, O.; Morris, H. S.; Grandquist, J. R.; Qin, Z.; Stone, E. A.; Tivanski, A. V.; Grassian, V. H. *J. Phys. Chem. A* **2015,** *119* (19), 4489-4497.

38. Mauchly, J. W. *Annals Math. Stat.* **1940,** *11,* 204-209.

39. Schuttlefield, J. D.; Cox, D.; Grassian, V. H. *J. Geophys. Res.: Atm.* **2007,** *112* (D21303).

40. Baltrusaitis, J.; Usher, C.; Grassian, V. H. *Phys. Chem. Chem. Phys.* **2007,** *9* (23), 3011-3024.

41. Ferreto, L.; Glisenti, A. *J. Molec. Cat. A.* **2002,** *187,* 119-128.

42. Lutz, H. D.; Möller, H.; Schmidt, M. *J. Molec. Struc.* **1994,** *328,* 121-132.

43. Navea, J. G.; Chen, H.; Huang, M.; Carmichel, G. R.; Grassian, V. H. *Environ. Chem.* **2010,** *7,* 162-170.

44. Madejová, J.; Komadel, P. *Clays and Clay Minerals* **2001,** *49,* 410-432.

45. Namduri, H.; Nasrazadi, S. *Corrosion Sci.* **2008,** *50,* 2493-2497.

46. Konan, K. L.; Peyratout, C.; Bonnet, J.-P.; Smith, ; Jacquet, ; Magnoux, ; Ayrault,. *J. Coll. Interf. Sci.* **2007 ,** *307 ,* 101–108.

47. White, S. C.; Case, E. D. *J. Materials Sci.* **1990,** *25* (12), 5215-5219.

48. Tomeczek, J.; Palugniok, H. *Fuel* **2002,** *81,* 1251-1258.

49. Srinivasachar, S.; Helble, J. J.; Boni, A. A. *Progress in Energy Combustion Science* **1990,** *16,* 281-292.

50. Zinder, B.; Furrer, G.; Werner, S. *Geochimica et Cosmochimica Acta* **1986,** *50* (9), 1861-1869.

51. Remucal, C. K.; Sedlak, D. L. In *Aquatic Redox Chemistry;* Tratnyek, P. G. . G. T. J. . H. S. B., Ed.; American Chemical Society: Washington, DC, 2011; Vol. 1071, p 177.

52. Lesko, D. M. B.; Coddens, E. M.; Swomley, H. D.; Welch, R. M.; Borgatta, J.; Navea, J. G. *Phys. Chem. Chem. Phys.* **2015,** *17,* 20775-20785.

53. Srinivas, ; Sarin, M. M.; Kumar, A. *Biogeochemistry* **2012,** *110* (1), 257-268.

54. Usher, C. R.; Michel, A. E.; Grassian, V. H. *Chem. Revi.* **2003,** *103* (12), 4883–4940.

55. Borgatta, J.; Navea, G. *WIT Trans. Ecol. Environ.* **2015,** *198,* 155-166.

56. Al-Abadleh, H. A. *RSCAdv*., **2015**, 5, 45785–45811.

Chapter 3: Fate of aqueous iron leached from tropospheric aerosols during atmospheric acidic processing: study of the effect of humic-like substances

Abstract

Humic-like substances (HULIS) are complex organic molecules that can be found in the atmosphere as components of tropospheric aerosols or suspended in atmospheric water. HULIS are chelating agents and oxidation-reduction species. Therefore these substances can affect the availability of aqueous iron, a heavy metal commonly leached from atmospheric particulate matter upon acidic processing. Specifically, chelating properties allow HULIS to remove aqueous iron from atmospheric water, while their redox properties can alter iron speciation. Ultimately, wet deposition of soluble iron can be influenced not only by HULIS but also by other ubiquitous atmospheric cations. In this work, we investigated the effect of HULIS on iron leached from atmospheric particles in the presence of aluminium ions, an environmentally abundant cation also chelated by HULIS. Colorimetric methods were used to examine the cation exchange (C.E.) of aluminium ions with both iron (II) and (III) ions in humic acids, a model system for HULIS. An effective chelation of aqueous phase iron with humic acids was observed during suspension experiments, with aqueous iron removed from aqueous phase into a HULIS complex. In addition, the redox properties of humic acids showed no oxidation of iron (II) after chelation by humic acid, but a fraction of iron (III) was reduced into the more bioavailable iron (II). Cation exchange with aluminium suggests that bioavailable iron (II) ions chelate with HULIS in a combination of exchangeable and non-exchangable iron, with a higher proportion of exchangeable iron incidence. Additionally, HULIS interaction with iron (III) ions shows chelating properties as well a reduction potential, producing aqueous and chelated iron (II) ions.

Introduction

In recent years it has become increasingly clear that atmospheric organic substances, in particular water soluble compounds, significantly impact the properties of tropospheric aerosols.[1] One of the most ubiquitous classes of water-soluble organic compounds in the atmosphere are HUmic-LIke Substances (HULIS). [2,3] While lighter in molecular weight than soil and aquatic humic substances, HULIS present many characteristics that resemble aquatic humic acids.[4] Like aquatic and terrestrial humic acids, HULIS are polymeric, polyacidic materials, containing a multicomponent mixture of aromatic and aliphatic compounds with carbonyl, hydroxyl, methoxyl, and carboxyl terminal groups [4]. Taraniuk and collaborators found that HULIS, like humic acids, are powerful chelating agents, impacting the chemistry of aerosol particles.[5] Additionally, terrestrial and aqueous humic substances are dominant redox-active species;[6] thus, it is supposed that HULIS also play an important role in reduction-oxidation mechanisms of atmospheric pollutants.[6] Yet, many environmental implications of HULIS on trace atmospheric metals, such as heavy metal mobility,[7] ligand promoted aerosol dissolution,[8] and the redox effect,[6] have not yet been explored.

The acidic functional groups of HULIS can bind to a variety of metals ions. This chelating property is particularly important for iron, a limiting nutrient for phytoplankton in the ocean.[9,10] Chen and Grassian proposed that ligand-promoted solubility of iron from atmospheric aerosols may play a significant role in mobilizing Fe from atmospheric dust compared with acidic processing alone.[8] Ultimately, van der Perk suggests that the humic-metal complexation enhances metal solubility,[11] effectively partitioning heavy metals from tropospheric aerosols into atmospheric water. Thus, HULIS strong chelating functional groups may influence the ligand promoted solubility and further mobility of iron in tropospheric aqueous systems.[12] However, the

transport and binding strength of the HULIS-Fe system is closely dependent on the relative replaceability of exchangeable cations, as described by Scheffer and Schachtschabel.[13] For instance, HULIS chelate Fe^{3+} with a slightly higher strength than that of Al^{3+}, and overall higher binding strength than Fe^{2+}, approximately following the stability order of $Fe^{3+} > Al^{3+} > Fe^{2+}$.[13] Thus, a system with large excess of Al^{3+} can effectively displace any exchangeable Fe^{2+} complexated by HULIS, but might not be as effective in exchanging with Fe^{3+}. Yet, metal binding to HULIS can take place on non-exchangable sites,[14] making the cation exchange (C.E.) process more convoluted.

In addition to the metal binding, HULIS are important redox agents.[6] In fact, electrochemical potentials determined by Aeschbacher and collaborators suggest that humic substances will be primarily reducing agents for iron.[6] While Fe^{3+} is the most abundant species of iron in tropospheric aerosols,[12,8] the presence of HULIS in atmospheric water can reduce iron to bivalent species, which is more bioavailable. Although the reduced form of iron can be exchanged by surrounding Al^{3+} in the aqueous phase, there are only a few investigations on the influence of Fe^{2+} and Fe^{3+} binding to organic substances under atmospherically relevant conditions.[15] In order to better understand the redox effect of HULIS on atmospheric aqueous iron, along with the effect of Al^{3+} on this process, we carried out cation exchange studies with Al^{3+} under atmospherically relevant conditions for both Fe^{3+} and Fe^{2+} on humic acids, a proxy for atmospheric HULIS.

Experimental Methods

Materials

The HULIS solution was prepared by adding 10.0 mg of humic acid (HA) (Sigma-Aldrich) as a proxy, in a 10.0 mL acidic solution of iron standard. Standard solutions of Fe^{3+} were prepared by dissolving iron (III) nitrate nonahydrate $(Fe(NO_3)_3)\cdot 9H_2O$ (Sigma-Aldrich), into 2% nitric acid

solution until the desired concentration was reached. The Fe^{2+} standards were prepared from a 1000 ppm stock solution of Fe^{2+}, obtained by dissolving primary standard Fe $(NH_4)_2(SO_4)_2 \cdot 6H_2O$ (Sigma-Aldrich) in an aqueous 0.01 M HCl solution. All HA solutions on iron standard were prepared to a final pH of 4.

Cation exchange was carried out by adding aluminium chloride, $AlCl_3$ (Alpha-Aesar), in a large excess, for a final concentration of 0.1% w/w in Al^{3+}. The final solution was acidified to a final pH of 2, and filtered for detection.

Methods

HA suspension with iron standards were incubated at room temperature overnight and non-chelated aqueous iron was selectively analyzed colorimetricaly with o-phenanthroline (Alpha-Aesar) for Fe^{2+} and potassium thiocyanate (Sigma-Aldrich) for Fe^{3+}, forming the absorbing complexes shown in reactions (3.1) and (3.2) (*vide infra*). Interferences from HULIS chromophores are within the margin of error of the methods, as all solutions are diluted 10 times upon analysis, minimizing any humic substance interference. In addition, both o-phenanthroline and thiocyanate iron complexes have a maximum of absorption at 525 nm and 490 nm, respectively, well above the maximum of absorption of soluble humic acid at 220 nm. The analysis of Fe^{3+} with potassium thiocyanate showed a slight HULIS interference, although quantification was still possible under experimental conditions. Non-chelated Fe^{2+} is selectively analysed via colorimetry, without interference from iron chelated by HULIS, as the {HULIS- Fe^{2+}} and {HULIS- Fe^{3+}} complexes are favoured over the o-phenanthroline complex with Fe^{2+} and thiocyanate complex with Fe^{3+}. The extraction of iron from HULIS by the colorimetric ligand has been shown to be slow, allowing the analysis of only aqueous iron (II):[16]

$$Fe^{2+}(aq) + 3\ o-phen\ (aq) \rightleftharpoons \{Fe(o-phen)_3\}^{2+}(aq) \quad (3.1)$$

$$Fe^{3+}(aq) + SCN^{-}\ (aq) \rightleftharpoons \{FeSCN\}^{2+}(aq) \quad (3.2)$$

The colorimetric analysis of humic acid samples in iron standards after overnight passivation allowed the evaluation of the HULIS-iron complex formation.

To investigate the C.E., $AlCl_3$ was added to the HULIS-Fe complex solutions until a final concentration of 0.1% w/w of Al^{3+}. Aluminum binds strongly with HULIS. In the presence of an excess of aluminum, the C.E. leads to the following reaction:

$$\{HULIS - Fe^{n+}\}(aq) + Al^{3+}(aq) \rightleftharpoons \{HULIS - Al^{3+}\}(aq) + Fe^{n+}(aq) \quad (3.3)$$

where n is the oxidation state of iron (2+ or 3+). Reaction (3.3) leaves iron available in aqueous phase for colorimetric analysis with o-phenanthroline or potassium thiocyanate (reactions (3.1) and (3.2)). Exchanged iron was determined immediately after the addition of Al^{3+}, as cation exchange takes place instantaneously.[11] However, based on the stability order of the HULIS-metal complex (*vide supra*),[13] reaction (3.3) is not favored for iron in the oxidation state n=3+, limiting the concentrations of Fe^{3+} exchanged. Finally, for the C. E. reaction (3.3) to be analytically useful, the concentration of Al^{3+} needs to be in excess, so the equilibrium is displaced towards the products. The pH of C.E. used for all the iron concentrations examined was pH = 2, acidified by the hydrolysis of $AlCl_3$.

Results and discussion

Characterization of HULIS Model System and HULIS-metal binding

The solutions of HULIS, as well as HULIS treated in an iron standard solution before and after cation exchange (C. E.) with aluminum, were dried and analyzed using an attenuated total reflection (ATR), in a germanium crystal (Pike Technologies), with a Fourier transformed infrared

(FTIR) spectrometer (Thermo, 6700). A thin film of the humic sample, with and without metal complexation, were prepared by applying the aqueous sample onto the ATR crystal and placed in a dry air purged sample compartment; as water evaporated, a thin film of the HULIS/HULIS-metal sample was homogeneously deposited on the surface of the ATR crystal. Figure 3.1 shows three different FTIR spectra: humic acid with no iron or aluminium (HULIS), humic acid in a 15 ppm solution of Fe^{2+} (HULIS+Fe^{2+}), and the solution after C. E. (HULIS+Al^{3+}). All FTIR spectra are averages of 100 scans with a 4 cm^{-1} resolution.

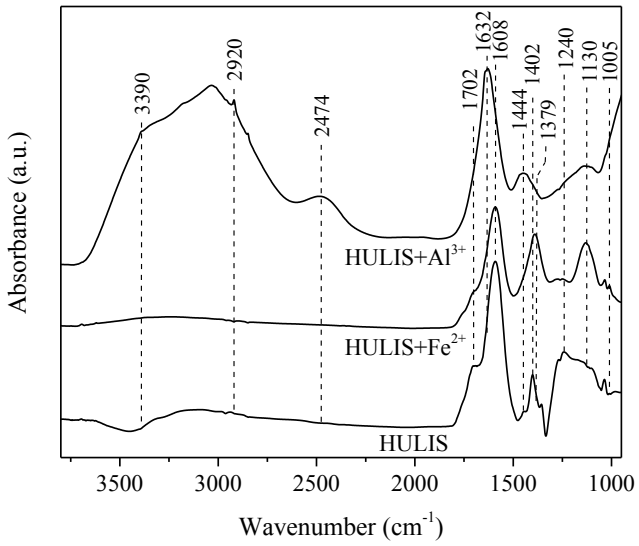

Figure 3.1. Infrared spectrum of dried HULIS solutions (ATR-FTIR). Bottom spectra: aqueous phase of HULIS; middle spectra: HULIS in a 15 ppm solution of Fe^{2+} standard; top spectra: HULIS after cation exchange with Al^{3+}.

ATR-FTIR of the samples revealed a typical spectra of humic materials. The broad and intense peak ranging from 3100 to 3500 cm^{-1} is assigned to O-H stretching with inter- and intra-molecular hydrogen bonding characteristic of polymeric alcohols, phenols, and carboxylic acids.[4],[17] The relatively high intensity of this OH band in the presence of aluminum indicates that humic materials are protonated due to the acidic environment during C. E. This equilibrium protonation

can also be observed in the clear band at 2920 cm^{-1}, assigned to a C-H stretching vibration of aliphatic acids and in the band centered at 2474 cm^{-1} that is typical for protonated carboxylic acids.[4]

The carboxylic band at 1608 cm^{-1} shows a shift of $\Delta\nu$ = 24 cm^{-1} in excess of aluminum, indicating that metal chelation takes place with binding to the carboxylic group.[4,17] In addition, there is a significant shift ($\Delta\nu$ = 42 cm^{-1}) in the C-H aromatic ring stretch, at 1402 cm^{-1},[18] suggesting that aromatic rings also participate in the metal chelation process. Given the low concentrations of iron chelated in HULIS, no significant shifts are observed in the carboxylic or aromatic bands. However, iron chelation is indicated by a significant Fe-O band growth at 1379 cm^{-1} along with a small but observable band at 1030 cm^{-1} assigned to the Fe-OH stretch.[19] In addition, the disappearance of the peak at 1240 cm^{-1} as metals are added to the HULIS mixture indicates that OH in phenol groups also participate in the chelation of metals.[18,20] The peak assignment for HULIS solutions is summarized in Table 3.1.

Table 3.1. ATR-FTIR peak assignments for HULIS samples

Frequency (cm^{-1})	Assignment	Reference
3390	H-bonded OH	[4, 17, 21]
2920	C-H stretching of aliphatic acids	[4, 17, 21]
2474	O-H ν_{as} (COOH)	[17, 20]
1702	C=O ν_{as} (COOH)	[4, 17, 21]
1608/1638	C=O ν_{as} (COO^-)	[17]
1450-1370	C-H ring stretch	[18]
1379	Fe-O stretch	[19]
1240	Ph-OH and Ph-COOH stretch	[20, 21]
1130	C-O(C=O) ν_{as}	[21]
1030	Fe-O stretch	[19]
1005	C-H Polysaccharides stretch	[4, 21]

Figure 3.2 shows the UV-Vis spectrum (Perking-Elmer Lambda 35) of the humic fractions with and without metal treatment. In general, the HULIS proxy shows a strong absorbance, mainly in the UV range, from 190 nm to 400 nm, due to the presence of aromatic chromophores. Upon addition of metal, the UV absorptivity around 220 nm decreases, characteristic of the π-π^* transitions in substituted benzenes or polyphenols.[22] This relative loss of absorptivity indicates that aromatic C=C undergoes distortion and electron density loss during metal binding. Some red shift is also observed as shoulders when iron and aluminum are chelated by the humic substance, supporting that the aromatic rings in HULIS also participate in metal chelation, as suggested by the FTIR spectra.

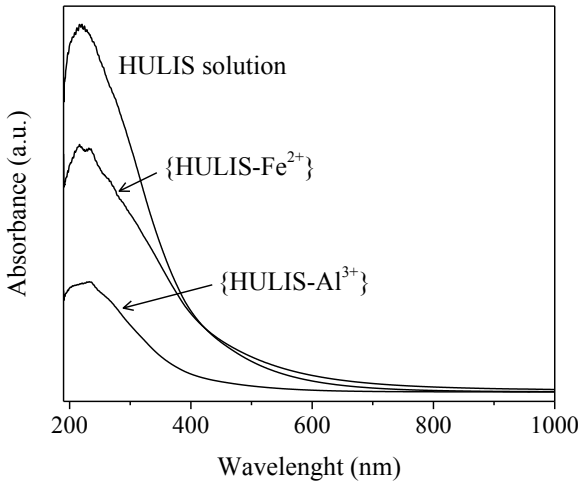

Figure 3.2. UV-Vis spectrum of humic solutions. Aqueous phase humic acid (HULIS solution); humic acid in 15 ppm of iron (II) standard ({HULIS-Fe^{2+}}); humic acid after cation exchange with excess of aluminum (III) ({HULIS-Al^{3+}}).

An elemental analysis of the organic sample (CHN analyser, Costech Instruments) revealed an organic composition of the humic substance used as HULIS proxy of (38±2)%, (3.34±0.08)%, (0.84±0.05)%, in carbon, hydrogen, and nitrogen, respectively. The C/H and C/N rations are similar to those proposed by the Steelink humic monomer.[23] In addition, X-ray fluoresce (XRF) spectroscopy (Bruker) showed the presence of trace metals in the untreated sample, with a relatively large presence of iron. Analysis with atomic absorption spectrophotometer (Perkin Elmer) showed (1.07±0.03)% total iron, with estimated concentration of calcium, strontium, and titanium <0.5%, and copper, nickel, zinc, phosphorous and sulphur <0.05%.

HULIS chelation of iron

As suggested by spectroscopic evidence in the preceding section, HULIS chelates iron and aluminum using different functional sites. Under atmospherically acidic conditions of pH below 4,[24] the moderately acidic functional groups of HULIS tend to be protonated, with a variable

negative density charge.[11] In addition, at pH below 4, aqueous phase aluminum is predominantly in the Al^{3+} form.[11] These conditions promote the C. E. as described by reaction (3.3), in which a large excess of Al^{3+} will exchange with exchangeable Fe^{2+} or Fe^{3+}. Cation exchange is a relatively fast process, which allows for the instantaneous analysis of iron in solution upon C. E.

Figure 3.3 shows the fraction of Fe^{2+} standard chelated by HULIS with respect of the initial concentration of Fe^{2+} standard ($[Fe^{2+}]_0$). It is clearly observed that, a significant fraction of the aqueous Fe^{2+} remains in solution as free Fe^{2+} after the equilibrium in reaction (3.4) has been reached:

$$\mathrm{HULIS}(aq) + \mathrm{Fe^{2+}}(aq) \rightleftharpoons \{\mathrm{HULIS - Fe^{2+}}\}(aq) \tag{3.4}$$

As the HULIS binding sites get occupied, the formation of the $\{\mathrm{HULIS - Fe^{2+}}\}$ complex reaches a limit given by the saturation of HULIS chelating sites. Under our experimental conditions, the HULIS chelating capacity reaches a maximum at a $[Fe^{2+}]_0$ threshold of around 10 ppm. Above this threshold concentration, a constant amount of Fe^{2+} will complex with HULIS.

Because HULIS is present in a relatively large concentration (1000 mg/L) with respect to $[Fe^{2+}]_0$, [HULIS] remains relatively constant over the course of the reaction. Thus, the equilibrium constant for equation (3.4) can be expressed as K'_{eq}, or the ratio between of remaining aqueous Fe^{2+} (free Fe^{2+}) with respect of $[\mathrm{HULIS - Fe^{2+}}]$:

$$K_{eq} = \frac{[\mathrm{HULIS - Fe^{2+}}]}{[\mathrm{HULIS}][\mathrm{Fe^{2+}}]} \Rightarrow K'_{eq} = [\mathrm{HULIS}]K_{eq} = \frac{[\mathrm{HULIS - Fe^{2+}}]}{[\mathrm{Fe^{2+}}]} \tag{3.5}$$

Upon saturation of HULIS chelating sites, the concentration of Fe^{2+} in aqueous phase ($[Fe^{2+}]$) increases with $[Fe^{2+}]_0$, and thus the K'_{eq} decreases. The change in the equilibrium constant is, therefore, driven by the ratio between the concentration of {HULIS-Fe^{2+}} and free Fe^{2+} (K'_{eq}) and it is represented in the insert of Figure 3.3.

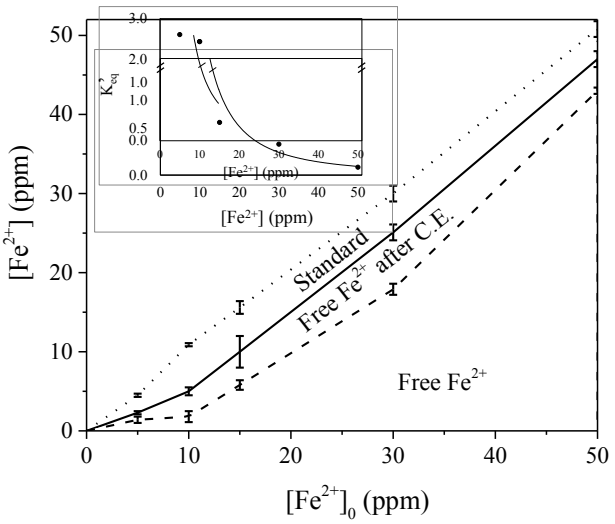

Figure 3.3. Free and exchangeable Fe^{2+} from a HA suspension on Fe^{2+} standards. The area under the dashed line represents the concentration of Fe^{2+} remaining in solution (free Fe^{2+}) after HULIS chelation of available iron. The area under the solid line represents free Fe^{2+} after the addition of 0.1% w/w of Al^{3+}, once C. E. has been completed. Finally, the area under the dotted line represents the total Fe^{2+} present in solution before the addition of HULIS. The insert represent the ratio between the concentration of {HULIS-Fe^{2+}} and free Fe^{2+}. Each point is the mean of triplicate measurements and the error bars represent the standard deviation.

This HULIS-Fe^{2+} complex is highly soluble, increasing the environmental mobility of iron. Therefore, HULIS complexing of iron is a significant factor in the transport and wet deposition of atmospheric iron. However, based on the Schefer and Schachtschabel[13] chelate stability, the ubiquitous Al^{3+} can break the HULIS-Fe^{2+} interaction for the most favored {HULIS-Al^{3+}}, particularly under Al^{3+} excess, a common environmental occurrence during tropospheric aerosol dissolution.

Figure 3 shows the relative increase of aqueous free Fe^{2+} after the addition of Al^{3+} to the {HULIS-Fe^{2+}} solution. However, the amount of Fe^{2+} measured after C. E. (solid line) is less than the original amount of Fe^{2+} added (dotted line). Since no Fe^{3+} was detected, suggesting no oxidation of Fe^{2+} by HULIS, some Fe^{2+} must remain chelated in HULIS. This indicates two types of binding sites, one exchangeable and one non-exchangeable. The non-exchangeable sites of

HULIS are favored as suggested by the binding observed for 5 ppm of Fe^{2+} solutions, where exchanged Fe^{2+} was only (1.2±0.2) ppm, or around 27% of the initial aqueous Fe^{2+}. In general, the non-exchangeable iron in HULIS, $[Fe^{2+}]_{inx}$, seems to be fairly constant as evidenced by the relatively constant slope of free iron after C.E, particularly after the 10 ppm threshold. Under our experimental conditions, $[Fe^{2+}]_{inx}$ reaches a maximum of 5 ppm for every $[Fe^{2+}]_0$ examined, after which non-exchangeable sites are no longer available.

Increasing the initial concentration of aqueous Fe^{2+} to concentration above a threshold of 10 ppm, where both HULIS sites become saturated, showed a relatively higher iron recovery (ϕ_R):

$$\phi_R \approx \frac{[Fe^{2+}]_0 - [Fe^{2+}]_{inx}}{[Fe^{2+}]_0} \tag{3.6}$$

Where iron recovery is the ratio of the concentration of free Fe^{2+} after C.E. divided by the initial concentration of Fe^{2+}, $[Fe^{2+}]_0$. At relatively higher concentrations of initial Fe^{2+}, the percentages of exchanged iron rose to 29%, 65%, 75% and 92% for initial Fe^{2+} concentrations of 10 ppm, 15 ppm, 30 ppm, and 50 ppm, respectively. Clearly, $[Fe^{2+}]_{inx}$ depends on the concentration of HULIS. Higher concentrations of HULIS in atmospheric water will increase the non-exchangeable sites available to irreversible chelate Fe^{2+}. Thus, it can easily be shown that the C.E. yield can be expressed by the logical statement in equation (3.7):

$$[Fe^{2+}]_0 > [Fe^{2+}]_{inx} \leftrightarrow \phi_R = 1 - \frac{[Fe^{2+}]_{inx}}{[Fe^{2+}]_0} \tag{3.7}$$

Equation (6) implies that as $[Fe^{2+}]_0$ increases, the iron recovery will be larger.

HULIS redox of iron

Incubation of HULIS with Fe^{2+} yields only Fe^{2+}, either chelated or free. In contrast, suspension of HULIS in Fe^{3+} standard yields both Fe^{2+} and Fe^{3+}. Table 3.2 shows the effect of HULIS proxy

suspension in a solution of 18 ppm of Fe^{3+} standard. Here, HULIS reduction potential is enough to form free Fe^{2+}.

Table 3.2. HULIS on Fe^{3+} standard.

$[Fe^{3+}]_0$ (ppm)	$[Al^{3+}]$ (% w/w)	Free $[Fe^{3+}]$ (ppm)	Free $[Fe^{2+}]$ (ppm)	Free $[Fe]_{total}$ (ppm)
18	0	1.8±0.2	1.2±0.4	2.0±0.6
	0.1	2.1±0.2	2.4±0.7	4.5±0.9
30	0	0.12±0.09	1.1±0.1	1.2±0.2
	0.1	2.4±0.9	5.6±0.5	7.9±1
50	0	0.60±0.09	2.5±0.5	3.1±0.6
	0.1	3.0±0.7	6.7±0.3	9.7±1

Once again, HULIS does not chelate all the amount of iron available. Before C. E., a significant fraction of Fe^{3+} standard, $[Fe^{3+}]_0$, is chelated by HULIS. In addition, 4-7 % of the Fe^{3+} standard is converted into free Fe^{2+}. The chelation and exchange of iron by HULIS can be summarized as follows:

$$\mathrm{HULIS(aq)} + \mathrm{Fe^{3+}\ (aq)} \rightarrow \{\mathrm{HULIS - Fe^{3+}}\}(\mathrm{aq}) \quad (3.8)$$

$$\mathrm{HULIS(aq)} + \mathrm{Fe^{3+}\ (aq)} \rightarrow \mathrm{Fe^{2+}(aq)} + [\mathrm{HULIS}]^{+}(\mathrm{aq}) \quad (3.9)$$

$$\mathrm{HULIS(aq)} + \mathrm{Fe^{2+}\ (aq)} \rightarrow \{\mathrm{HULIS - Fe^{2+}}\}(\mathrm{aq}) \quad (3.10)$$

$$\{\mathrm{HULIS - Fe^{n+}}\}(\mathrm{aq}) + Al^{3+}(aq) \rightleftharpoons \{\mathrm{HULIS - Al^{3+}}\}(\mathrm{aq}) + \mathrm{Fe^{n+}} \quad (3.11)$$

In equation (3.9) HULIS transfers an electron to reduce Fe^{3+}, producing Fe^{2+} which can be chelated by HULIS. As a consequence, the charge density of HULIS becomes less negative, diminishing its capacity to effectively bind iron. However, given the higher stability of the

{HULIS-Fe^{3+}}, iron recovery is lower than observed in the presence of only Fe^{2+}, around 25 % total iron recovery, which is significantly lower than the recovery observed for Fe^{2+} alone. This is supported by the low amount of Fe^{3+} exchanged in every concentration examined, consistent with the chelate stability observations of Schefer and Schachtschabel.[13] Given the large excess of Al^{3+}, this low C.E. suggests that Fe^{3+} binds to HULIS stronger than Al^{3+}. Most iron exchanged corresponds to the reduced species of iron, Fe^{2+}. In fact, the concentration of aqueous Fe^{2+} increases significantly after C.E. with Al^{3+}.

As the $\{\text{HULIS} - Fe^{3+}\}$ complex is more stable, a higher HULIS induced mobility is expected for Fe^{3+} than that for Fe^{2+}. In fact, given the values of $[Fe^{2+}]_{inx}$ (5 ppm) under our experimental conditions, it can be assumed that Fe^{3+} is the larger fraction of non-exchangeable iron that results from the interaction of HULIS with Fe^{3+} standard. However, HULIS can also decrease the relative concentration of Fe^{3+} in atmospheric water in favor of Fe^{2+}.

Atmospheric Implications

In the past decade, it has been suggested that atmospheric acidic processing of tropospheric aerosols leaches mostly Fe^{3+} into atmospheric water.[25] However, the presence of HULIS suggests that a fraction of aqueous Fe^{3+} leached from atmospheric dust will undergo reduction to form the bioavailable Fe^{2+}. In addition, the higher solubility of the HULIS-Fe complexes can induce further aerosol dissolution. Thus, the presence of HULIS will not only increase the concentration of aqueous iron in atmospheric water but increase the transport of iron species in the troposphere. Ultimately, since Fe^{2+} is bioavailable and a limiting phytoplankton nutrient, during atmospheric acidic processing HULIS can induce and/or boost plankton blooms.

Nonetheless, environmental factors can directly impact the role of HULIS in the transport, chelation, and reduction of iron. Cations such as Al^{3+}, also leached from acidic dissolution of

atmospheric dust, induce cation exchange, which partition Fe^{2+} to the aqueous phase. Given that both metals, aluminum and iron, are common components of atmospheric dust, HULIS will induce a relatively larger concentration of Fe^{2+} than initially expected in the aqueous phase of tropospheric water.

References

1. Fuzzi, S.; Andreae, M. O.; Huebert, B. J.; Kulmala, M.; Bond, T. C.; Boy, M.; Doherty, S. J.; Guenther, A.; Kanakidou, M.; Kawamura, K.; Kerminen, V. M.; Lohmann, U.; Russell, L. M.; and Pöschl, U. *Atmos. Chem. Phys.* **2006,** 2017-2038.
2. Decesari, S.; Fuzzi, S.; Facchini, M. C.; Mircea, M.; Emblico, L.; Cavalli, F.; Maenhaut, W.; Chi, X.; Schokolnik, G.; Falkovich, A.; Rudich, Y.; Claeys, M.; Pashynska, V.; Vas, G.; Koutchev, I.; Vermeylen, R.; Hoffer, A.; Andreae, M. O.; Tagliavini, E.; Moretti F. and Artaxo, P. *Atmos. Chem. Phys.* **2006***,* 6, 375-402.
3. Salma, I.; Ocskay R. and Láng, G. G. *Atmos. Chem. Phys.,* **2008**, 8, 2243-2254.
4. Graber, E. R. and Rudich, Y. *Atmos. Chem. Phys.,* **2006,** 6, 729-753.
5. Taraniuk, I.; Rudich Y.; and Graber, E. R. *Environ. Sci. Technol.,* **2009,** 43, 1811-1817.
6. Aeschbacher, M. Sander M. and Schwarzenbach, R. P. *Environ. Sci. Tech.,* **2010,** 44, 87-93.
7. Paciolla, M. D.; Davies G. and Jansen, S. A. *Environ. Sci. Technol. ,* **1999**, 33, 1814-1818.
8. Chen H. and Grassian. V. H. *Environ. Sci. Technol.,* **2013**, 47, 10312−10321.
9. Martin, J. H. *Paleoceanography,* **1990**, 5, 1-13.
10. Moore, J. K.; Doney, S. C.; Glover D. M. and Fung, I. Y. *Deep-See Res. Part II-Top. Stud. Oceanogr.,* **2002**, 49, 463-507.
11. van der Perk, M. Soil and water contamination, Leiden, The Netherlands: CRC Press, **2014**.
12. Lippold, H.; Evans, N. D. M.; Warwick P. and Kupsch, H. *Chemosphere,* **2007**, 67, 1050-1056.
13. Scheffer F.; Schachtschabel, P.. Lehrbuch der Bodenkunde, Stuttgart, Germany: Enke Verlag, **1989**.
14. Zhou, P.; Yan H. and Gu, B. *Chemosphere,* **2005**, 58, 1327-1337.
15. Holmes B. J. and Petrucci, G. A. *Environ. Sci. Technol.,* **2006**, 40, 4983-4989.
16. Fujisawa, N.; Furubayashi, K.; Fukushima, M.; Yamamoto, M.; Komai, T.; Ootsuka K. and Kawabe, Y. *Humic Sub. Res.,* **2011**, 8, 1-6.
17. Xiao-hong, G.; Guang-hao C. and Chii, S. *J. Environ. Sci.* **2007**, 19, 438-443.
18. Dorado, J.; Zancada, M. C.; Lamendros G. and López-Fando, C. *J. Plant Nutr. Sci.,* **2003,** 166, 31-38.

19. Colombo, C.; Palumbo, G.; Sellitto, V. M.; Rizzardo, C.; Tomasi, N.; Pinton R. and Cesco, S. *Soil Sci. Soc. Am. J.,* **2011,** 76, 1246-1256.
20. Jayaganesh S. and Senthurpandian, V. K. *Asian J. Earth Sci.,* **2010,** 3, 130-135.
21. Cowen S. and Al-Abadleh, H. A. *Phys. Chem. Chem. Phys.,* **2009,** 11, 7838-7847.
22. Baduel, C.; Voisin D. and Jaffrezo, J. L. *Atmos. Chem. Phys.,* **2009,** 9, 5949-5962.
23. Steelink, C. in *Humic Substances in Soil, Sediment, and Water*, New York, Wiley, **1985**, 457-476.
24. Seinfeld J. H. and Pandis S. N. Atmospheric Chemistry and Physics: From Air Pollution to Climate Change, **2006,** Hoboken, N. J.: Wiley.
25. Kyei, P.; Rubasinghege G. and Graasian, V. H. *Abstr. Pap. Am. Chem. S.,* **2011,** 241.

Chapter 4: Heterogeneous chemistry of atmospheric particles: experimental design of surface photochemistry and surface-free radical reactions

Abstract

During atmospheric transport, the chemical and physical properties of aerosols particles are changed by reactive agents like solar radiation, and hydroxyl radicals (OH), among others. This weathering process is called "aging," and can cause the degradation of the aerosol particles, changes in surface characteristics of particles, or the formation of secondary products. The most reactive tropospheric aging species is the hydroxyl radical which is responsible for the oxidation of atmospheric aerosols. Previous studies investigating the synergistic reaction between free radicals and surface-bound species on tropospheric aerosols have used UV-light to generate hydroxyl radicals. While these reactions have begun to show the oxidizing properties of OH radicals, the use of light in the experiments have made it difficult to discern whether the oxidation was due to the radical species or the interactions between the semiconducting surface and light. For a more holistic view of the aging process involving solar radiation and OH radicals, two state-of-the-art reaction systems were designed. The objective of this chapter is to introduce the design of these two systems, along with preliminary experiments performed to validate the experimental approaches. The experiments allowed for the successful quantification of photoactive gaseous products in a photochemical heterogeneous reaction. This was achieved by determining that the residence time of photoactive gases, in the irradiation reactor where they are produced, is significantly lower than the time required for them to photo-decay. In addition, for the first time a system was tested to determine the oxidative properties of oxygen free radicals in the absence of UV-light.

Introduction

During their atmospheric lifetime aerosols experience an "aging" process. The aging process consists of a variety of chemical and physical processes that change the aerosol properties.[1] The aging process is caused by the interaction of aerosols with light, atmospheric acids (hydrogen chloride, nitric acid, or sulfuric acid among other acids), and/or trace atmospheric compounds (sulfur dioxide, nitrogen oxides, or hydroxyl radicals, among other).[2-4] During the atmospheric lifetime, the aging process facilitates chemical reactions and the degradation of aerosols. Recent studies indicate that the most powerful aerosol aging agent is the hydroxyl radical (OH).[1] Hydroxyl radicals facilitate the oxidation of organic aerosols or organic compounds coating inorganic aerosol particles such as mineral dust or fly ash.[5]

Previous studies have looked at the reaction of hydroxyl radicals and organics adsorbed onto the surface of semiconductor metal oxides, to serve as proxies for atmospheric aerosols.[5] Hydroxyl radicals have been seen to oxidize trace atmospheric compounds chemisorbed on the surface of aerosol particles and they have been seen to decrease the fraction of organic components by fragmentation of the substrates.[6, 7] However, the experimental design that has been previously used depended upon the generation of hydroxyl radicals through the irradiation of ozone and vapor with UV light. The use of light in the radical generation process makes it difficult to discern whether the reaction products are caused by interactions with the hydroxyl radicals or if they are due to electron hole pairs from the excited semiconducting metal oxide surface: [8]

$$Substrate(a) + h\nu \xrightarrow{j} Product(a) \tag{4.1}$$

$$Substrate(a) + O(\,^3P) \xrightarrow{k} Product(a) \tag{4.2}$$

where *Substrate*(a) signifies any adsorbed trace gas, j is the heterogeneous photochemical kinetic constant, and k is the reaction kinetic rate constant in a reaction with free radical O(^{3}P).

The objective of this work is to describe the strategy designed to better understand the kinetics of aerosol aging by separating the reactions above. This strategy consists of two different state-of-the-art experimental setups: (1) the first experimental setup looks into examines the heterogeneous photochemistry of chemisorbed nitrate (NO_3^-) onto semiconductors such as TiO_2;[9] (2) the second experimental setup investigates the interface reactions between chemisorbed compounds and free radicals generated as a cold plasma, in the absence of light. Therefore, reactions (4.1) and (4.2) can be examined independently for an overall kinetic constant, *k*:

$$k = k_{h\upsilon} + j \tag{4.3}$$

This chapter describes the experimental setup and validation of the experimental conditions that allows the separation of the influence of electron-hole pair from the influence of the hydroxyl radicals. The first part will examine the effectiveness of a state-of-the-art heterogeneous photochemistry experiment to determine photoactive gas-phase products. The second part of this chapter will describe the development of a new plasma reactor system for the generation of free radicals for the reaction with chemisorbed organics.

Experimental Methods: Heterogeneous Photochemistry

The objective of the following study is to determine the photochemical rate of degradation of photoactive gaseous products as they travel through an illuminated region, and contrast that reaction rate with the diffusion time of photoactive gaseous products as they are transported out of the irradiated region. To determine the influence of light on molecules adsorbed onto semiconducting metal oxide surface, we examined the gas phase products of the following unbalanced reaction of nitrate on TiO_2:[10]

$$NO_3^-(a) + H^+(a) \xrightarrow{h\nu} NO(g) + NO_2(g) + N_2O(g) + HONO(g) \tag{4.3}$$

where (a) represents adsorbed species. From the products listed above, NO_2 and HONO degrade in the presence of light:

$$NO_2 + h\upsilon \xrightarrow{j_{NO_2}} NO + O \tag{4.4}$$

$$HONO + h\upsilon \xrightarrow{j_{HONO}} NO + OH \tag{4.5}$$

A state of the art system was utilized, combining parallel FTIRs to look at products adsorbed to the surface and the gas products that were produced (figure 4.1). There are three main components to the experimental setup: the gas generator, the photochemical cell, and the gas analysis chamber.

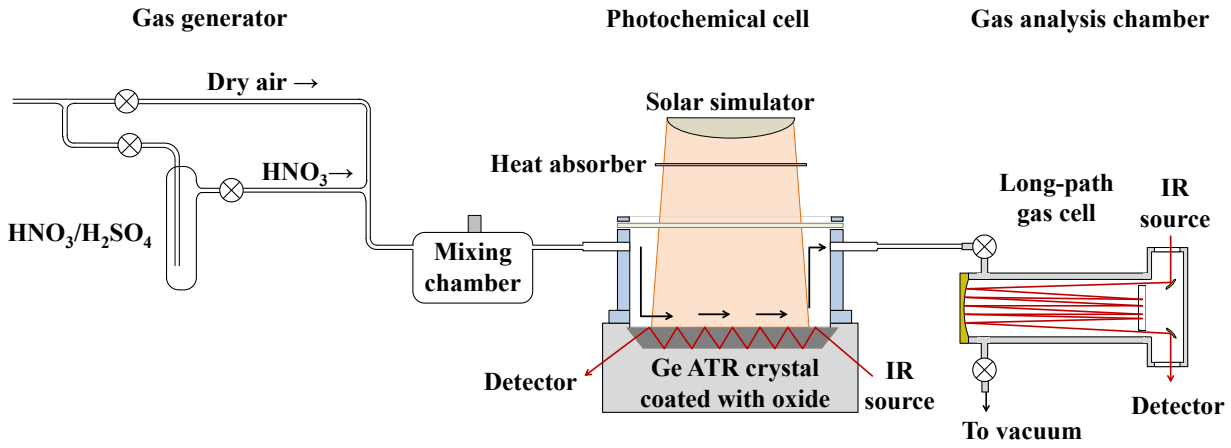

Figure 4.1. Schematic diagram of the experimental set-up used in these studies.

The typical experiment is described in a recent publication by our research group.[9] Briefly, gaseous HNO_3 is generated by flowing of purified dry air through a 3:1 mixture of sulfuric acid: nitric acid and in to the photochemical cell. The photochemical cell consists of a Teflon chamber enclosing an attenuated total reflection (ATR) germanium crystal (Pike Technologies), which supports the nitric acid on TiO_2 sample to be studied and it is coupled to a Fourier Transformed infrared (FTIR) spectrometer (Thermo, 6700). The photochemical cell reaction chamber is coupled

to a sample/vacuum line and an IR long-path cell for gas-phase product analysis. A UV-Vis transmission window (Ultran®) on top of the Teflon chamber allows broadband irradiation from the light source (ORIEL, 500 W). As adsorbed nitric acid photolysis takes place, gaseous products desorb and diffuse out of the irradiation region and towards the gas analysis chamber.

In order to determine gas-phase products, the experiment requires that all desorbed products diffuse to the gas cell. However, gaseous products desorbed from the surface pass through an irradiated region. If the photoactive gases NO_2 and HONO take more time to diffuse than the time it takes to for them to react, the concentration that reaches the long-path cell, where they are analyzed and quantified, can be considerably depleted. It is, therefore, paramount to determine the residence time of the gases inside the photochemical cell (τ_{res}) and compare it to their lifetime under the irradiation conditions (τ).

Findings of the Study: Heterogeneous Photochemistry

Irradiance Profile in the Photochemical Cell

The spectral absolute irradiance was determined by placing a calibrated spectroradiometer (Oriel USB4000) at the ATR crystal level. The UV-Transmission window on the photochemical cell effectively blocks radiation below 290 nm, a threshold wavelength above which the absolute irradiance sharply increases. The spectral profile in the region of interest is shown in Figure 4.2A, along with the absorption cross-sections for NO_2 and HONO, the two photoactive species with overlap between the light source and the absorption profile. Figure 4.2B represents the spatial distribution of the light source beam at the level of the ATR crystal, where heterogeneous photochemistry takes place. The broadband light intensity distribution was measured across the ATR crystal using a calibrated photocell. The light intensity shows a Gaussian profile, with

obscuration effects at each end of the crystal. At the center of the crystal, the irradiance of the light beam has an average output of approximately 1.10 kW m^{-2}, or 1.2 of air mass 1 (AM1), similar to the irradiance at the top of Earth's atmosphere.

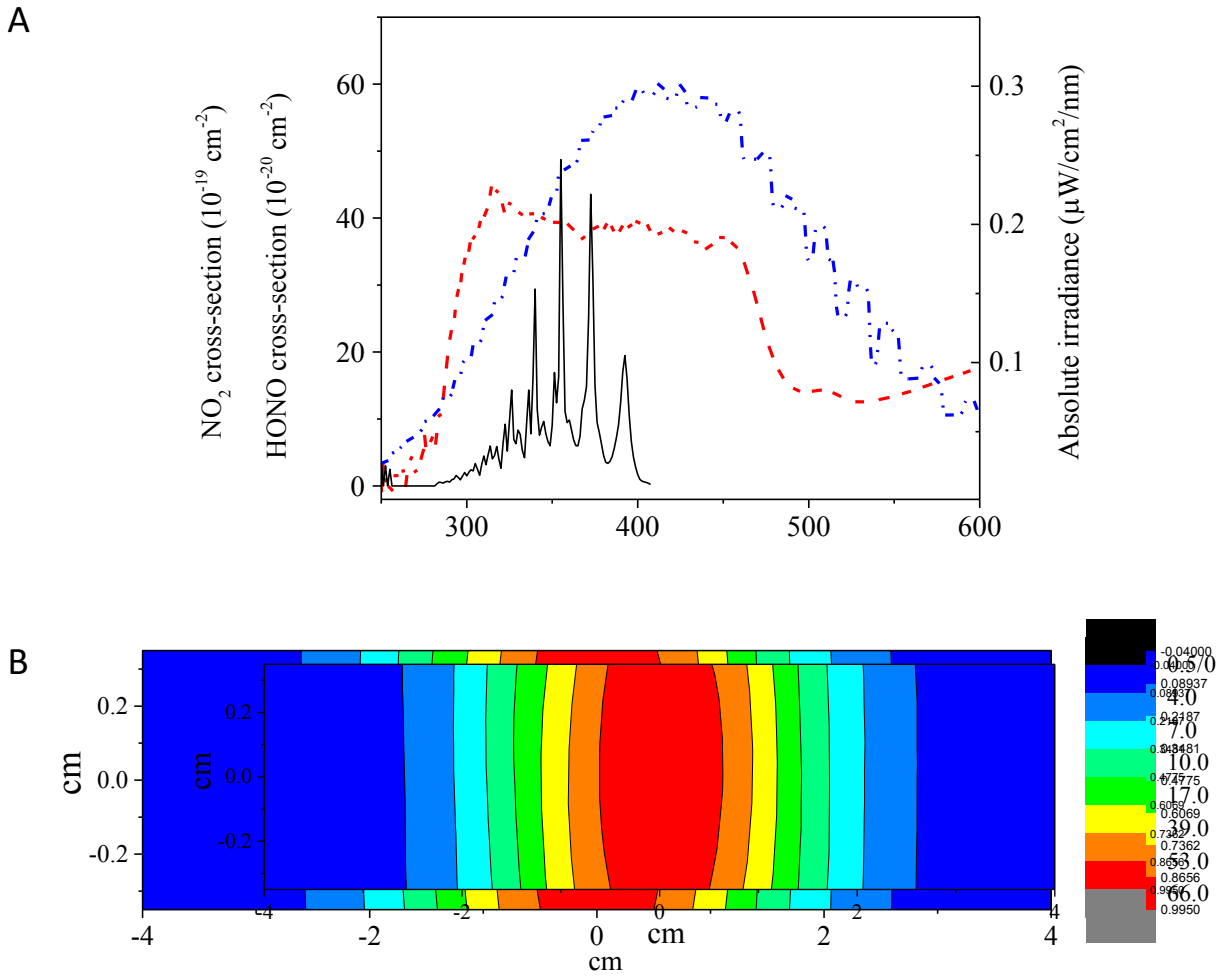

Figure 4.2: (A) Solar simulator spectral irradiance (red line) at the bottom of the photochemistry cell. As a reference, the absorption cross sections of nitrous acid (black line), nitrogen dioxide (blue line) are also shown. (B) Solar constant profile in the chamber at the ATR crystal. The total area of irradiance shows a Gaussian profile with a radius of approximately 5 cm at the ATR crystal level.

Diffusion of Gas Products as Function of Photochemical Lifetime

As shown in Figure 4.2, only the absorption cross-sections for NO_2 and HONO overlap with the radiation in the photochemical cell, while N_2O photolysis below the cutoff of the

photochemical cell window.[12] Thus, only NO_2 and HONO can decay during their residence time (τ_{res}) in the photochemical cell, as they diffuse out of the irradiation region:

The first order photolysis rate constant, *j*, can be calculated using equation (4.6) for any gaseous product "*p*" from the overlap between the measured absolute irradiance and the known absorption spectral data:

$$j_p = \int_{\lambda} \sigma_p \phi_p I_S d\lambda \tag{4.6}$$

where σ_p and ϕ_p are the wavelength dependent absorption cross-section and dissociation quantum yield, respectively, for HONO or NO_2, and I_S is the spectral actinic flux for the broadband radiation determined from the data of Figure 4.2.[8,9] The rate constants calculated from equation (4.6) are $j_{NO2} \approx 2.6\times10^{-2}$ s^{-1} and $j_{HONO} \approx 3.9\times10^{-3}$ s^{-1}.

In order to evaluate the photolysis of NO_2 and HONO, the residence time, τ_{res}, of these gases in the region of irradiation is estimated from the diffusivity coefficient for a binary system at low pressures, with gases diffusing through the main product, NO_2, using equation (4.7), and NO_2 initially diffusing through air and then self-diffusing:

$$(\Delta x)^2_{avg} = 6 D_{p-NO_2} \tau_{res} \tag{4.7}$$

where Δx is the average region of irradiation determined from the center of the irradiation region in Figure 2B, 2.75 cm, and D_{p-NO_2} is the diffusivity constant for the low pressure binary system of gas "*p*" through NO_2, determined with the Chapman and Enskog equation[13]

$$D_{A-NO_2} = \frac{2.66 \times 10^{-3} T^{3/2}}{P\, M_{p-NO_2}\, \sigma^2_{p-NO_2}\, \Omega_D} \tag{4.8}$$

With the molar mass $M_{p-NO_2} = 2\left[\left(1/M_p\right) + \left(1/M_{NO_2}\right)\right]^{-1}$, Ω_D the diffusion collision determined with the Lennard-Jones energy, σ_{p-NO_2} the characteristic length from molecule "*p*" to NO_2, T is

the reaction temperature of the reaction chamber, and P is the pressure of the system.[14] Thus, in order to minimize photolysis of gaseous photoactive products, the experimental conditions should follow equation (4.9), implying that the residence time must be smaller than the photolysis lifetime of product p, $\tau_p > \tau_{res}$:

$$\frac{1}{j_p} > \frac{(\Delta x)^2_{avg}}{6D_{p-NO_2}} \tag{4.9}$$

The diffusivity constant of NO_2 through air, calculated from equation (4.7), was $D_{NO2} = 1.0\times10^4$ Torr cm^2 s^{-1}, while HONO diffusivity has been estimated to be $D_{HONO} = 96$ Torr cm^2 s^{-1}.[15] Using these diffusion constants, the residence times at the end of the heterogeneous photolysis of nitric acid (equation 4.3) were calculated using equation (4.7), yielding τ_{res} values of approximately 14 ms and 15 ms for NO_2 and HONO, respectively. Thus, τ_{res} are smaller than their photolysis lifetimes, calculated to be approximately 256 s and 39 s for NO_2 and HONO, respectively. Therefore, residence time does not allow enough time for significant photochemical reactions to occur during the first order kinetic regime:

$$\frac{d[NO_2]}{dt} = -j[NO_2] \Longrightarrow Ln\left(\frac{[NO_2]_{\tau_{res}}}{[NO_2]_0}\right) = -j\cdot\tau_{res}$$

$$\frac{[NO_2]_{\tau_{res}}}{[NO_2]_0} = e^{-j\cdot\tau_{res}} \tag{4.10}$$

Since, under our experimental conditions $[NO_2]_{\tau_{res}}/[NO_2]_0 \cong 0.999$, there is no measurable photochemical decay of products during their residence time in the photochemical cell.

Experimental Methods: Plasma Study

Atmospheric processing simulation involving free radicals reacting with chemisorbed substrates have been limited to non-photoactive species because free radicals have been generated through photochemical processes.[16] Here we present an alternative method, where free radicals are

generated through a radio frequency discharge in a non-thermal plasma. A non-thermal, or cold plasma, is a gas dissociated to form gaseous ions and neutral species such as atoms, molecules and free radicals. In particular, non-thermal plasmas are plasmas where the ions and neutral particles are at a much lower temperature than that of the electrons ($T_e >> T_p$).[17] In fact, at low pressures around 100 mtorr, the ions and neutral particles are at room temperature.[18]

Generating the free radicals with plasma offers two advantages: first, photoactive surfaces and substrates can be investigated without interference from photochemical reactions; second, the kinetics of the reaction can be studied in situ by monitoring surface species. This project proposes to investigate the mechanism and kinetics of the heterogeneous oxidation of chemisorbed hydrocarbons by $O(^3P)$ radicals in a non-thermal plasma, as a step towards OH reactions on chemisorbed species on aerosol particles.

Plasma reaction system.

The plasma is generated in a low pressure system (20 to 150 mtorr) and directed to a reaction chamber for $O(^3P)$ reactions with organic species chemisorbed on aluminum oxide (Al_2O_3). Here, the main role of the solid support is to prevent the vaporization of volatile organic compounds of interest.[19] A custom made radio frequency generator and coil by Manitou Systems Inc., was used to generate 100 watts of radiofrequency discharge, enough energy to ionize dry and humidified oxygen gas. The reaction system is set up as follows:

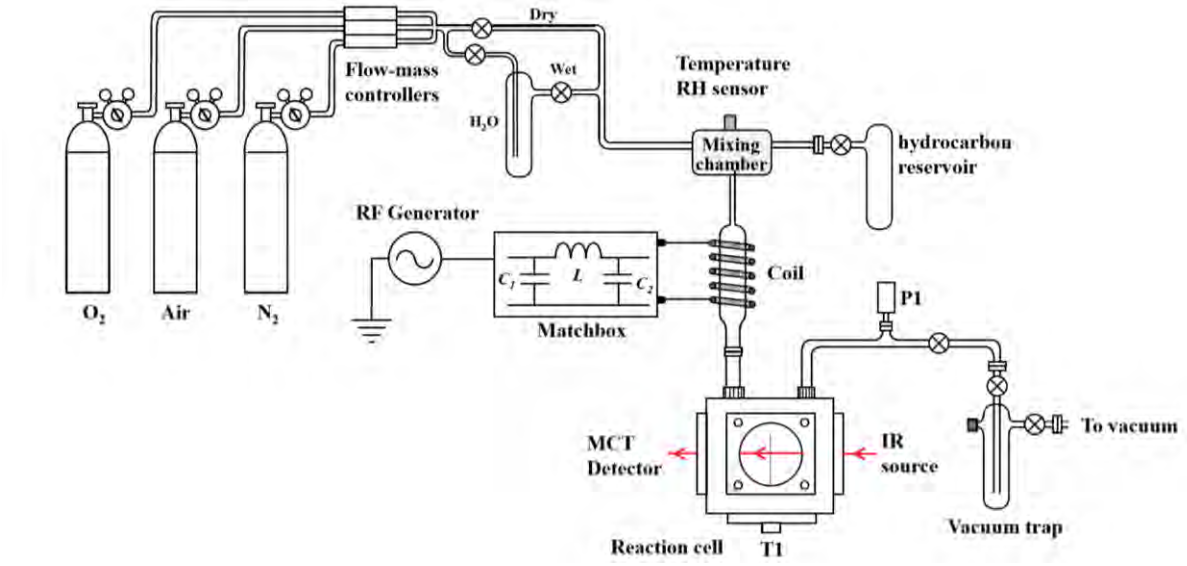

Figure 4.3: The reaction system for experimentation with the cold hydroxyl radical plasma.

The aluminum reaction chamber receives the plasma plumes and directs it towards the organic compound chemisorbed onto Al_2O_3. The chamber, shown in Figure 4.4, consists of a custom made cube that fits in the sample compartment of an FTIR spectrometer. The reaction chamber has a sample holder that consists of a tungsten grid (20 μm wire diameter) that holds the sample and allows for transmission FTIR. The plasma inlet was designed so that the plasma would flow across the sample. As shown in Figure 4.3, two quartz windows on opposite sides of the reaction chamber allow for UV-Vis detection, and two barium fluoride (BaF_2) windows allow for IR analysis. The reaction system was designed as follows:

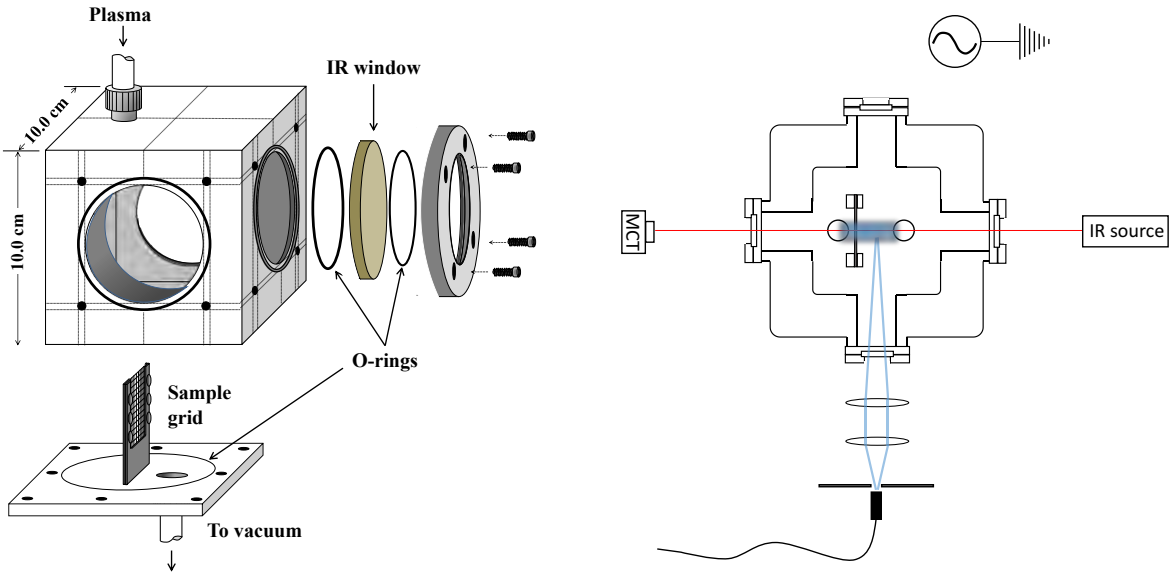

Figure 4.3. Left: Diagram of the aluminum reaction chamber designed for plasma reactions. Right: the detection system used that contained an IR source and windows, and an ocean optics spectrometer with quartz windows detecting the plasma emission lines (represented with blue lines).

Preliminary tests were performed using the plasma coil and concentric tubes to determine the optimum conditions to generate $O(^3P)$ in the reaction site. This optimization was performed by using a UV-Vis spectrometer equipped with a fiber optics (Ocean Optics). The pressure of the system was modified by adjusting the amount of oxygen that flowed in to the system, and monitoring the emission intensity for $O(^3P)$ at 777.06 nm, the ground state of neutral atomic oxygen.[20, 21]

The pressure dependence optimization in Figure 4.4 shows an increase in the intensity of the $O(^3P)$ emission line as a function of pressure, with a maximum near 35 mtorr.

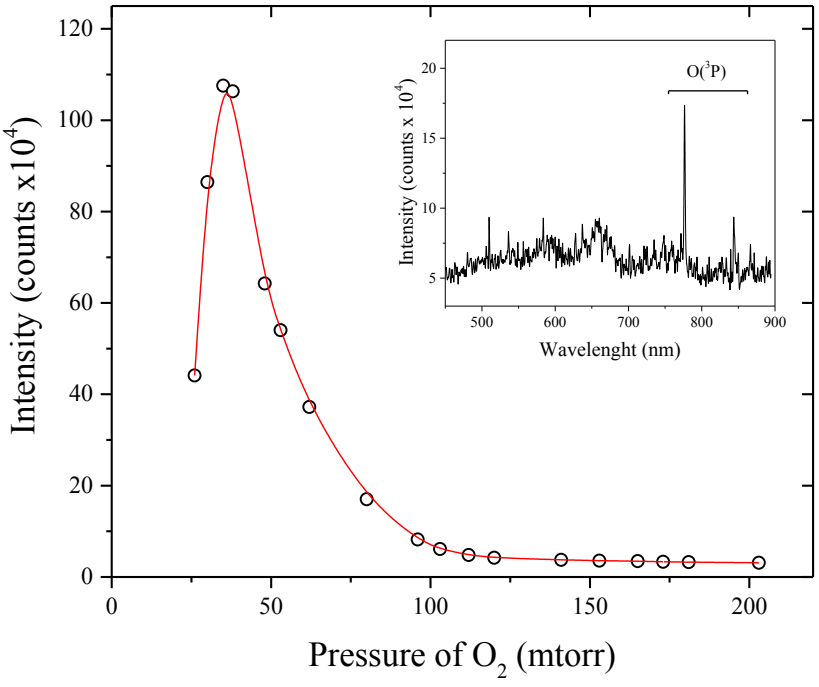

Figure 4.4. The emission intensity as it relates to the pressure of oxygen gas within the reaction system. The insert shows the two lines corresponding to O(^{3}P) resulting from a plasma discharge in 98 mtorr O_2.

This increase in plasma species correlates with the number of gas molecules that could be dissociated during the discharge. However, beyond 35 mtorr the collision frequency increases between plasma species causing recombination and the weakening of the plasma. A pressure of 35 mtorr was found as optimum for the plasma discharge.

Generation of a reaction surface and a complete preliminary test of the reaction system.

Preliminary experiments were conducted by adsorbing benzaldehyde (C_7H_6O) onto Al_2O_3. The sample was prepared by mixing a slurry of aluminium oxide and benzaldehyde, the slurry was then deposited on the tungsten grid, and secured within the sample holder. The sample holder was then installed in the reaction chamber and placed under vacuum to remove any weakly adsorbed benzaldehyde (physisorbed). The desorption of products was monitored by taking FTIR

transmission scans until there were no spectral changes observed. An optimized plasma was then allowed to flow through the system and the spectral changes were monitored using the aforementioned FT-IR.

Heterogeneous Reaction: Adsorbed Benzaldehyde + $O(^3P)$

In a typical experiment, infrared scans are collected as the reaction between plasma and adsorbed benzaldehyde takes place, with the infrared spectra referenced to C_7H_6O(a) on Al_2O_3 (blank). Thus, the infrared spectrum at the beginning of the experiment, right before the substrate is exposed to plasma (t=0), is a horizontal line. As the experiment progresses, new surface-bound products should appear as "positive" spectral features with respect to the infrared spectrum at t=0, while depression bands will correspond to functional groups that have been removed or altered during the reaction.

There were many spectral changes observed upon plasma treatment. In Figure 4.5, the blue infrared spectrum at the bottom of the figure represent the spectral features of benzaldehyde chemisorbed on Al_2O_3. The black horizontal line is the initial spectrum before reaction with the adsorbed benzaldehyde (blue spectrum) as a blank. Finally, the red spectrum corresponds to the functional groups produced after 14 minutes of reaction with $O(^3P)$.

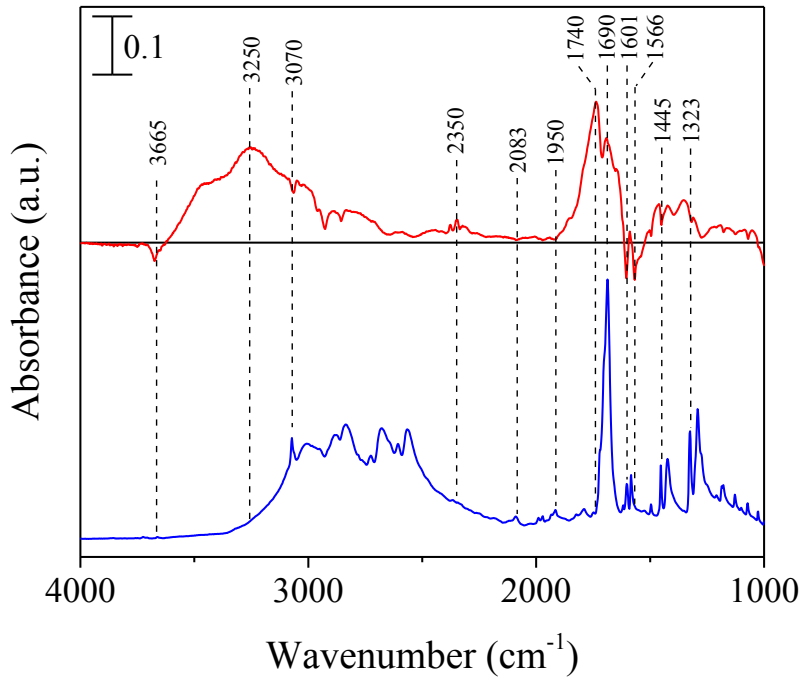

Figure 4.5. The change in IR spectra for plasma treated benzaldehyde. The blue represents the spectrum of benzaldehyde before plasma treatment and red represents the spectrum after plasma treatment. A benzaldehyde background was taken and has been subtracted.

The bands that corresponded to the C-H and C-C stretching modes of the aromatic ring of benzaldehyde, at 3070 cm^{-1}, at 1601 cm^{-1}, 1445 cm^{-1}, and at 1323 cm^{-1}, decreased after 14 minutes of plasma exposure. The decreased number of aromatic infrared features is likely due to $O(^3P)$ reacting with the aromatic ring. Conversely, a significant increase in the hydroxyl band was observed around 3250 cm^{-1}. There were also spectral changes observed that indicated a growth of carbonyl groups at 1740 cm^{-1}. The increase in the bands that corresponded to hydroxyl groups and carbonyl groups represented the oxidation of the organic species by the $O(^3P)$ plasma. Furthermore, the functionalization with NO_2 groups was also observed at 2350 cm^{-1}, likely due to the presence of air in the plasma.

The preliminary study showed an initial increase in the functionalization by oxygen containing groups up to 10 minutes of reaction. As can be seen in Figure 4.6, after 10 minutes the

functionalization decreased likely due to the removal of unstable groups by continued plasma treatment.

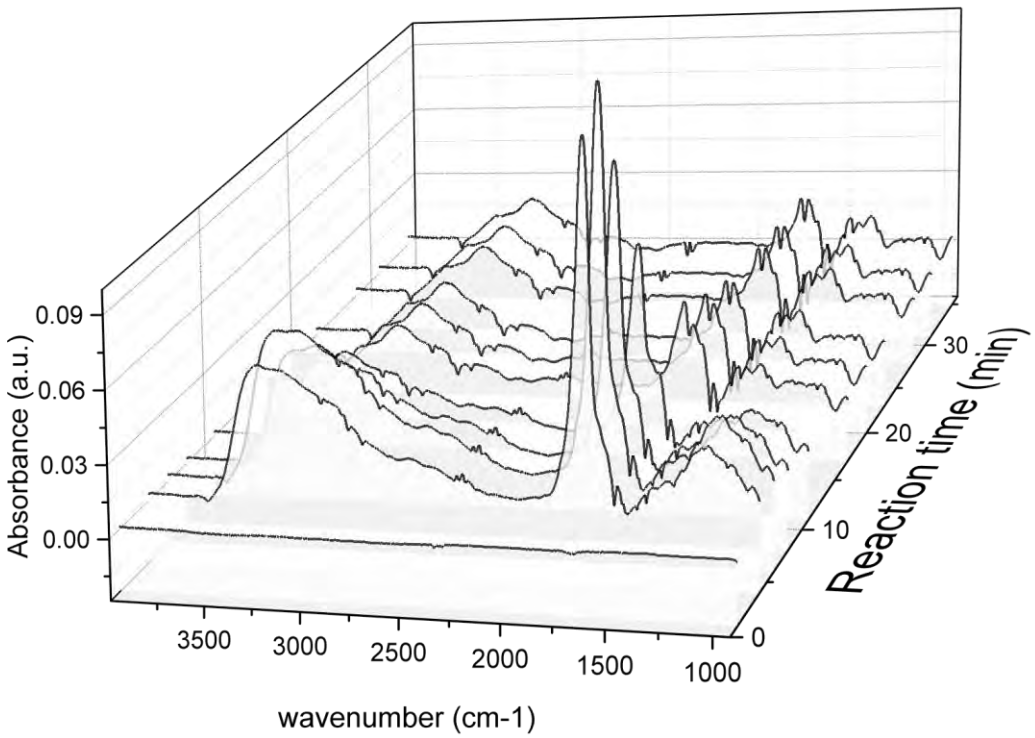

Figure 4.6. The IR spectra of plasma treated benzaldehyde, with a subtracted benzaldehyde background. The spectra were taken at different time intervals, showing varied degrees of functionalization with respect to the duration of plasma treatment.

Atmospheric implications of new instrumentation.

Two state-of-the-art systems were designed to determine the reaction products generated in a simulated atmospheric aging process. To look at the interaction between hydroxyl radicals and organic molecules adsorbed to a semiconducting surface, a state of the art system was designed

and validated. The reaction system for plasma reactions was useful because it allowed for the in situ determination of reaction products. The reaction system will be useful for a variety of chemical studies that look at the reactions between radical species and solid surfaces. In addition, the characterization of a reaction system used in photochemical experiments allowed for the determination of the diffusion rate of gaseous products with respect to the experimental irradiance profile, which allowed us to determine that gas phase products did not undergo any further reactions due to light after desorption from the reaction surface.

References

1. Rudich Y., Donahue N. M., Mentel T.F. *Annu. Rev. Phys. Chem.***2007**, 58:321-52.
2. Chen, H. H.; Navea, J. G.; Young, M. A.; Grassian, V. H. *J. Phys. Chem. A.* **2011,** 115, 490-499.
3. Rubasinghege, G.; Elzey, S.; Baltrusaitis, J.; Jayaweera, P. M.; Grassian, V. H. *J. Phys. Chem. A. Letters* **2010**, *1*, 1729-1737.
4. Finlayson-Pitts, B. J.; Raff, J. D.; Njegic, B.; Kamboures, M. A.; Chang, W.; Dabdub, D.; Gerber, R. B. *Abstr. Pap. Am. Chem. S.* **2009**, *237*, 177-177.
5. Donahue, N. M.; Henry, K. M.; Mentel, T. F.; Kiendler-Scharr, A.; Spindler, C.; Bohn, B.; Brauers, T.; Dorn, H. P.; Fuchs, H.; Tillmann, R.; Wahner, A.; Saathoff, H.; Naumann, K. H.; Mohler, O.; Leisner, T.; Muller, L.; Reinnig, M. C.; Hoffmann, T.; Salo, K.; Hallquist, M.; Frosch, M.; Bilde, M.; Tritscher, T.; Barmet, P.; Praplan, A. P.; DeCarlo, P. F.; Dommen, J.; Prevot, A. S. H.; Baltensperger, U. *Proc. Nat. Acad. Sci.* **2012**, 109 (34), DOI: 10.1073/pnas.1115186109
6. George, I. J. and Abbatt, J. P. D. *Nature*, **2010**, 2, 713–722 doi:10.1038/nchem.806
7. Houle, F. A.; Hinsberg, W. D.; Wilson, K. R. *Phys Chem Chem Phys*. **2015**;17(6):4412-23
8. Paulson, Suzanne. *Int. J. Chem. Kinet.* **1992,** 24, 0538-8066.
9. Fujishima, A.; Zhang, X.; and Tryk, D. A. *Elsvier.* **2008,** 12, 515-582.
10. Haller, I. *J. Am Chem Soc.* **1978**, 100: 8050-8055.
11. Lesko, D. M. B.; Coddens, E. M.; Swomley, H. D.; Welch, R. M.; Borgatta, J.; Navea, J. G. *Phys. Chem. Chem. Phys.* **2015,** *17,* 20775-20785.
12. Sander, S. P.; Friedl, R. R.; Golden, D. M.; Kurylo, M. J.; Moortgat, G. K.; Wine, P. H.; Ravishankara, A. R.; Kolb, C. E.; Molina, M. J.; Finlayson-Pitts, B. J.; Huie, R. E. No. 15. Jet Propulsion Laboratory: Pasadena, **2006**
13. Wall, K. J., Schiller, C. L., and Harris, G. W. J. *Atmo. Chem.* **2006**, 55(1), 31-54.
14. Poling, B. E., Prausnitz, J. M. and O'Connell, J. P. (**2001**). The Properties of Gases and Liquids, 5th Edn. McGraw-Hill, New York.
15. Massman, W. J. *Atmos. Env.* **1998**. 32 (6), 1111-1127.
16. Browne, E. C.; Franklin, J. P.; Canagaratna, M. R.; Massoli, P.; Kirchstetter, T. W.; Worsnop, D. R.; Wilson, K. R.; Kroll, J. H. *J. Phys. Chem. A* **2015**, 119, 1154-1163.
17. Tang, M. J., Cox, R. A., Kalberer, M. *Atmos. Chem. Phys.* **2014**, 14, 9233-9247.

18. Gambús, G.; Patiño P. and Navea J. *Energy & Fuels*. **2002**, 16, 172-176
19. Schuttlefield, J.; Rubasinghege, G.; El-Maazawi, M.; Bone, J.; Grassian, V. H. *J. Am. Chem. Soc*. **2008**, *130*, 12210-12211.
20. Patiño, P.; Méndez, M.; Pastrán, J.; Gambús, G.; Navea, J.; Escobar, O.; Castro. A. *Energy & Fuels*. **2002**, 16(6), 1470-1475
21. Gambús, G.; Patiño, P.; Méndez, B.; Sifontes, A.; Navea, J.; Martín; P. and Taylor; P. *Energy &Fuels*. 2001, 15, 881-886

Chapter 5: General Conclusions

The iron dissolution experiments from fly ash showed that the source region influenced the quantity and speciation of iron leached. A complete combustion process created spherical fly ash particles that had iron predominantly in the oxidized form Fe(III). Of the samples observed, the United States fly ash showed the largest overall fraction of leached Fe which was likely due to the minerology of the combusted coal. However, the majority of iron leached was in the form of Fe (III) indicating that the combustion process was complete. The Indian and European fly ash showed significantly less Fe leach. However, for the European sample, a relatively large fraction of the iron leached was in the form of Fe (II) indicating that the combustion process was likely incomplete. In order to have a stimulatory effect on phytoplankton growth a larger fraction of Fe(II) would have to be deposited in the ocean.

Potentially increasing the fraction of Fe (II) provided by fly ash, the leached Fe (III) could be reduced by environmentally prevalent HULIS. Humic-like substances in a simulated aqueous aerosol have been seen to have a chelating and reducing effect on iron. The chelating effects of HULIS allow for the mobilization of iron within an aqueous environment, while the reductive effects of HULIS increases the amount of biologically available Fe(II).

Additionally, particles like fly ash contain variety of metal oxides and adsorbed organic molecules. Two experimental systems have been designed to look at the surface interactions of these particles with OH radicals and light. The experiments with hydroxyl radicals have shown the oxidative effects of radicals on organic molecules, and by characterizing the light distribution and diffusion rate of products we have verified that gas products do not undergo further reaction due to light.

JB
Skidmore College
May 11, 2016